

Modeling the Dynamics and Thermochemistry for the Outer Atmospheres of the Ultra-hot Jupiter WASP-121b

LILE WANG (王力乐)  ^{1,2} YIREN LIN (林伊人)  ^{1,2} JI WANG (王吉)  ³ AND FEI DAI (戴飞)  ⁴

¹ *The Kavli Institute for Astronomy and Astrophysics, Peking University, Beijing 100871, China*

² *Department of Astronomy, School of Physics, Peking University, Beijing 100871, China*

³ *Department of Astronomy, The Ohio State University, 100 W 18th Ave, Columbus, OH 43210 USA*

⁴ *Institute for Astronomy, University of Hawaii, 2680 Woodlawn Drive, Honolulu, HI, 96822, USA*

ABSTRACT

We present three-dimensional simulations of the ultra-hot Jupiter (UHJ) WASP-121b from the planetary surface to extended outflows, coupling hydrodynamics with consistent non-equilibrium thermochemistry, ray-tracing radiative transfer, and hydrodynamics using the GPU-accelerated Kratos framework. The fiducial model exhibits several atmospheric layers, including the lower atmospheres controlled by day-night circulation, and transonic photoevaporative outflows at higher altitudes shaped into two spiral arms by the stellar gravity and orbital motion effects. Different species could trace different regions: Fe probes rotation-dominated inner layers, Na maps dense spiral arms where recombination balances photoionization, and H α and He 10830 Å features trace progressively more extended, ionized gas. With spiral arm velocities reaching ~ 40 km s $^{-1}$ projected along the line of sight, this morphology explains observed high-velocity Na and H α absorption features without requiring significant super-rotation jet streams. Parametric studies reveal complex dependencies on stellar irradiation: enhanced FUV intensifies outflows and extends spiral arms spatially and kinematically, while EUV and X-ray expands spiral structures into attenuated, ionized regions. Stellar wind confinement compresses the dayside outflow and enhances metastable helium absorption. This work demonstrates that current and future transmission spectral observations that probe multiple species can provide important constraints on astrophysical environments of UHJs by comparing state-of-the-art simulations.

Keywords: Exoplanets(498), Exoplanet atmospheres(487), Exoplanet atmospheric composition (2021), Star-planet interactions (2177), Hydrodynamics (1963), Chemical reaction network models (2237)

1. INTRODUCTION

Ultra-Hot Jupiters (UHJs) represent an extreme class of gas giants with dayside equilibrium temperatures $\gtrsim 2000$ K, driven by intense stellar irradiation at orbital distances $\lesssim 0.1$ AU (Parmentier et al. 2018; Lothringer et al. 2018). These highly irradiated planets experience intense stellar fluxes that fundamentally shape their atmospheric structure, causing significant atmospheric inflation and lifting atmospheric layers to high altitudes (Arcangeli et al. 2018a; Komacek & Tan 2018). Extreme thermal conditions drive atmospheric chemistry into a regime where molecular bonds are dissociated, or even atoms could be ionized, resulting in atmospheres

composed predominantly of atomic and ionic species rather than intact molecules (Evans et al. 2017; Parmentier et al. 2018). This unique thermochemical state, combined with their tidally locked rotation that creates permanent dayside and nightside hemispheres, distinguishes UHJs from their cooler Hot Jupiter counterparts and makes them laboratories for studying planetary atmospheres under the most extreme conditions observable.

UHJs could serve as testbeds for atmospheric characterization techniques and validating theoretical models (Changeat et al. 2022; Mansfield et al. 2021). The temperature contrast between their permanent daysides and nightsides, often exceeding 1000 K, provides a natural laboratory for studying heat transport efficiency, atmospheric circulation patterns, and the role of magnetic fields in shaping planetary climates (Bell & Cowan

2018; Tan & Komacek 2019). Furthermore, the partially ionized nature of their atmospheres allows for direct detection of elemental species that remain locked in molecular form in cooler planets, enabling precise abundance measurements that inform planet formation theories and migration histories (Hoeijmakers et al. 2019; Lothringer et al. 2020).

Recent observational advances have revealed remarkable atmospheric details. The most extensively studied include WASP-121b ($T_{\text{eq}} \simeq 2358$ K; Evans et al. 2016), WASP-76b (e.g. Ehrenreich et al. 2020), WASP-189b (e.g. Lendl et al. 2020), and the hottest known exoplanet KELT-9b ($T_{\text{eq}} > 4000$ K; Gaudi et al. 2017; Hoeijmakers et al. 2019). High-resolution cross-correlation spectroscopy (HRCCS) has identified species including atomic metals such as Fe I, Fe II, Na I, V I (Seidel et al. 2019; Borsa et al. 2021), along with molecular signatures of CO and H₂O (Yan et al. 2022; Ramkumar et al. 2023). These observations frequently reveal temperature inversion layers in dayside atmospheres (Sheppard et al. 2017; Arcangeli et al. 2019), supersolar metallicities (Changeat et al. 2022; Pelletier et al. 2025), and significant line broadening indicative of rapid rotation and atmospheric dynamics, while nightside detections remain challenging due to cooler temperature (Stevenson et al. 2017).

General Circulation Models (GCMs) have served as the cornerstone of UHJ atmospheric theory for over a decade, successfully reproducing large-scale features such as equatorial jets and day-night temperature contrasts (Showman et al. 2009; Lee et al. 2022). However, these models largely rely on the vertical hydrostatic approximation and Local Thermodynamic Equilibrium (LTE), assumptions that could break down in the upper atmospheric layers where high-resolution spectroscopic observations are most sensitive. The hydrostatic equilibrium assumption becomes invalid above pressures of $\sim 10^{-5}$ bar, precisely the regions where atomic metal lines form and where atmospheric escape processes dominate. Furthermore, GCMs typically employ simplified chemical networks or equilibrium chemistry prescriptions that cannot fully capture the non-equilibrium photochemistry and ionization dynamics prevalent in the thermosphere. This limitation is compounded by numerical dissipation and coarse vertical resolution (often ~ 40 layers spanning the entire atmosphere), which artificially suppress vertically propagating modes and underestimate temperature gradients in the uppermost layers. Consequently, while GCMs excel at modeling the deep atmospheres, they are not fully adequate to interpret the spectral signatures that originate from the dynamic, non-hydrostatic thermosphere where the impact

by the host star, including heating, photochemistry, and hydrodynamic escape, collectively determine the observable atmospheric signature.

To address these limitations, we present a series of consistent three-dimensional UHJ simulations that couple non-equilibrium thermochemistry, ray-tracing radiation, and hydrodynamics using the Kratos GPU-accelerated simulation system (Wang 2025a,b). This approach solves the hydrodynamic equation using higher-order Godunov method, conserving the extensive quantities (mass, momentum, energy, and chemical species) across a three dimensional (3D) mesh. The Kratos framework leverages mixed-precision arithmetic on heterogeneous GPU architectures to achieve computational speeds $50 - 100\times$ faster than comparable CPU-based codes, enabling real-time evolution of chemical networks comprising over 30 species and ~ 190 reactions under full non-LTE conditions with GPU-optimized semi-implicit method with adaptive step size and error control (Wang 2025b). We implement a comprehensive photochemical model that includes XUV-driven heating, ionization balance, and radiative cooling from metal species, while the hydrodynamic solver captures transonic outflow characteristics of atmospheric escape. This multi-physics treatment allows us to simultaneously model the transition from the dense lower atmosphere (where GCMs are good at modeling) to the rarefied upper atmosphere where transmission observations could probe, providing a unified framework to interpret high-resolution transmission spectroscopy while predicting the outflow hydrodynamics and thermochemistry behaviors relatively accurately.

This paper is structured as follows. In §2, we provide a detailed description of the numerical framework, including the setup of our 3D hydrodynamic simulations, the comprehensive non-equilibrium thermochemical network, and the methodology for generating synthetic transmission spectra. §3 presents the analyses of the fiducial simulation, characterizing the structure, dynamics, and thermochemical composition of the modeled outflowing atmosphere, and linking these features directly to observable spectral signatures. §4 systematically explores the influence of key physical parameters, especially stellar high-energy flux and stellar wind characteristics, on the atmospheric escape process and its observational diagnostics. Finally, §5 concludes our major findings, discusses their implications for the interpretation of current and future observations of UHJs.

2. METHODS

The numerical framework employed in this work to model the ultra-hot Jupiter WASP-121b is implemented

using the GPU-accelerated Kratos simulation system (Wang 2025a,b). This system integrates modules for consistent non-equilibrium thermochemistry and ray-tracing radiative transfer, with algorithms specifically optimized for Graphics Processing Units (GPUs) to achieve the high computational performance required for 3D global simulations. The underlying physical mechanisms, including hydrodynamic escape driven by stellar irradiation (calibrated to the stellar type) and the interaction with stellar winds, are consistent with the modeling approach previously developed for other evaporating exoplanetary systems such as WASP-69b and WASP-107b (Wang & Dai 2021a,b). In the following subsections, we provide a comprehensive summary of the key methodological aspects, with the primary parameters for our fiducial model detailed in Table 1.

2.1. Geometry and Boundary Conditions

We conduct our simulations on a spherical polar grid (r, θ, ϕ) that is centered on the planet and co-rotates with its orbital motion. This coordinate choice is essential to accurately capture the complex dynamics of the atmospheric outflow, which is governed by the combined influence of planetary gravity, stellar gravity, and orbital forces (specifically the centrifugal and Coriolis forces arising in the non-inertial rotating frame). The computational domain spans the radial range from the planetary surface at $R_p = 19.6 R_\oplus$, out to an outer boundary at $R_{\text{out}} = 160 R_\oplus$. This extensive radial coverage ensures that all critical physical processes, from the dense lower atmosphere to the extended, escaping exosphere, are contained within the simulation volume. The initial mass density at the inner boundary is set to $\rho_{\text{in}} = 10^{-5} \text{ g cm}^{-3}$, which corresponds to $p_{\text{in}} = 0.83 \text{ bar}$ with the $T_{\text{eq}} = 2400 \text{ K}$ equilibrium temperature. The latitudinal (θ) and azimuthal (ϕ) domains cover the upper hemisphere ($0 \leq \theta \leq \pi, 0 \leq \phi \leq \pi$), with the polar axis oriented perpendicular to the orbital plane. The substellar point is fixed at $(\theta, \phi) = (\pi/2, 0)$. To reduce computational cost while preserving the dominant physical symmetries, we model only the region above the orbital plane and impose reflection symmetry across this plane for the lower hemisphere.

The numerical grid is designed to resolve the large density gradients expected in an escaping atmosphere. We employ a logarithmically spaced radial grid to provide enhanced resolution near the planetary surface, while the angular grids in θ and ϕ are uniformly spaced. Appropriate boundary conditions are applied at the domain limits. At the inner boundary ($r = R_p$), we impose a reflecting condition, representing the impermeable planetary surface (or the base of the simulated,

Table 1. Properties of the fiducial model for WASP-121b

Item	Value
Planet properties	
M_p	$368 M_\oplus (\simeq 1.16 M_J)^*$
R_p	$19.6 R_\oplus (\simeq 1.76 R_J)^*$
T_{eq}	2400 K
Stellar and orbit properties	
$[u_1, u_2]^{**}$	[0.33, 0.21]
Orbital semi-major axis a	0.026 AU
Impact parameter b	$0.1 R_*$
Simulation domain	
Radial range	$19.6 \leq (r/R_\oplus) \leq 160$ $[1 \leq (r/R_p) < 8.16]$
Latitudinal range	$0 \leq \theta \leq \pi/2$
Azimuthal range	$0 \leq \phi \leq 2\pi$
Resolution ($N_{\log r} \times N_\theta \times N_\phi$)	$128 \times 32 \times 128$
Radiation flux [†] [photon cm ⁻² s ⁻¹]	
2 eV (IR/optical)	2.3×10^{21}
3 4.9 eV (Soft FUV)	2×10^{19}
6 eV (FUV)	2×10^{18}
12 eV (LW)	1×10^{16}
20 eV (Soft EUV ionizing H)	4×10^{15}
60 eV (Hard EUV)	1×10^{14}
0.3 keV (Soft X-ray)	1×10^{14}
3 keV (X-ray)	3×10^{13}
Initial abundances [n_X/n_H]	
H_2	0.46
He	0.08
H_2O	3.6×10^{-4}
CO	2.4×10^{-4}
Na	5×10^{-6}
Mg	6×10^{-5}
Ca	4×10^{-6}
Fe	6×10^{-5}
Gr [‡]	1×10^{-19}
Dust/PAH properties [‡]	
r_{dust}	1 Å
$\sigma_{\text{dust}/H}$ (Effective specific cross section)	$3 \times 10^{-35} \text{ cm}^2$

NOTE— *: Mass and radius of the Jupiter.

**: Limb darkening parameters, see also Yang et al. (2021).

†: See §2.2 for the representation of each energy bin.

‡: Very-small PAH and refractory graphitic grains could still survive sufficiently refractory to survive in the high-temperature regions ($T > 1500 \text{ K}$; see also §2.2).

quasi-isothermal atmosphere). At the outer boundary ($r = R_{\text{out}}$), an outflow condition allows material to freely escape the domain. The polar boundaries at $\theta = 0$ are treated as polar wedges to avoid coordinate singularities. To mitigate the restrictive Courant-Friedrichs-Lowy (CFL) timestep limitation imposed by the convergence of azimuthal grid lines near the poles, we implement a mesh coarsening technique in the ϕ -direction

at high latitudes (see e.g. Nakamura et al. 2019; Müller et al. 2019). This approach maintains the conservation of mass, momentum, and energy while significantly improving computational efficiency.

For our fiducial model of WASP-121b, we initialize the atmosphere with an isothermal density profile corresponding to an equilibrium temperature of $T_{\text{eq}} = 2400$ K, consistent with its orbital distance of $a = 0.026$ AU from its F6V host star. Planetary gravity is treated as a point mass $M_p = 368 M_{\oplus}$ located at the origin of the spherical polar coordinate system. The host star, positioned outside the simulation domain at coordinates corresponding to the orbital distance, influences the system through three primary effects, (1) its gravitational pull, (2) the inertial forces (centrifugal and Coriolis) in the co-rotating frame, and (3) the injection of radiative flux and stellar wind material. Given the short orbital period, we further assume WASP-121b is tidally locked on a circular orbit, thus the rotational angular frequency of the simulation frame is identical to the orbital counterpart.

2.2. Non-LTE Thermochemistry

The intense high-energy radiation from the host star drives the atmosphere of WASP-121b far from local thermodynamic equilibrium (LTE). To model this, we discretize the stellar spectral energy distribution (SED) into eight representative energy bins, each responsible for distinct photochemical processes:

1. 2 eV (as a representative bin for $h\nu < 4.8$ eV photons): Infrared, optical, and near-ultraviolet radiation, responsible for continuum heating.
2. 4.9 eV (for $4.8 \text{ eV} < h\nu < 5.14 \text{ eV}$): Soft far-ultraviolet (FUV) photons that can destroy the neutral helium in the metastable triplet state He^* ($I_{\text{He}^*} = 4.8$ eV).
3. 6 eV (for $5.14 \text{ eV} < h\nu < 7.9 \text{ eV}$): Soft far-ultraviolet (FUV) photons capable of ionizing sodium ($I_{\text{Na}} = 5.14$ eV).
4. 12 eV (for $11.2 \text{ eV} < h\nu < 13.6 \text{ eV}$): Lyman-Werner (LW) band photons, primarily driving the photodissociation of H_2 and CO , and can also ionize key tracing metals like iron (Fe), magnesium (Mg), and calcium (Ca).
5. 20 eV (for $13.6 \text{ eV} < h\nu < 24.6 \text{ eV}$): Soft extreme-ultraviolet (EUV) photons that ionize atomic and molecular hydrogen (H and H_2).
6. 60 eV (for $24.6 \text{ eV} < h\nu < 0.1 \text{ keV}$): Hard EUV photons that additionally ionize helium (He).

7. 0.3 keV (for $0.1 \text{ keV} < h\nu < 1 \text{ keV}$): Soft X-ray photons.

8. 3 keV (for $h\nu > 1 \text{ keV}$): Hard X-ray photons.

The incident flux F in photon number per unit area per unit time. In $h\nu < 13.6$ eV energy bins, photon fluxes are adopted according to the F6V super-solar metallicity host star WASP-121 (Sing et al. 2024). For $h\nu > 13.6$ eV energy bins, the EUV and X-ray fluxes are calibrated to the data provided in Czesla et al. (2024). Fluxes of all relevant bands are listed in Table 1.

The simulations self-consistently couple ray-tracing radiative transfer for these energy bins with hydrodynamics and a comprehensive non-equilibrium thermochemical network using the Kratos multiphysics framework (Wang 2025a,b). The chemical network, building upon established models for irradiated atmospheres (e.g., Wang & Dai 2021a), has been expanded to include species and reactions critical for ultra-hot Jupiter conditions. It comprises 185 reactions, including photoionization, radiative and dielectronic recombination, collisional excitation/de-excitation, photodissociation, and associated heating and cooling processes. The network tracks 33 equivalent species, including the specific internal energy, plus 32 chemical species: e^- , H , H^+ , H^- , H_2 , H_2^+ , H_3^+ , He , He^+ , He^* , O , O_2 , O^+ , OH , OH^+ , H_2O^+ , H_2O , H_3O^+ , C , C^+ , CH^+ , CH , CO , Fe , Fe^+ , Na , Na^+ , Ca , Ca^+ , Mg , Mg^+ , and Gr (representing a trace population of refractory graphitic dust grains). Here, H^- is included as a prospectively significant source of continuum opacity in hot atmospheres (see e.g., Arcangeli et al. 2018b; Jacobs et al. 2022). Initial abundances, assuming a bulk metallicity approximately twice solar (Sing et al. 2024), are provided in Table 1. The associated stiff system of ordinary differential equations for the reaction network is solved efficiently using a semi-implicit integration scheme optimized for GPU architectures (Wang 2025b).

The inclusion of full non-LTE thermochemistry significantly increases the computational cost. A typical 3D simulation for WASP-121b requires ~ 22 hours of wall-clock time on two NVIDIA RTX 4090 GPUs to simulate ~ 200 hours of physical time. This duration is justified by the estimated dynamical timescale,

$$\tau_{\text{dyn}} \sim \frac{GM_p}{c_s^3} \sim 30 \text{ hr} \times \left(\frac{M_p}{1.18 M_{\oplus}} \right) \left(\frac{T}{10^4 \text{ K}} \right)^{-3/2}, \quad (1)$$

which, despite potential shear instabilities, is sufficient for the system to reach a quasi-steady state. We first run the simulations for 100 simulated hours with hydrodynamics only (turning off thermochemistry and radiation), letting the hydrodynamic profiles to adjust to

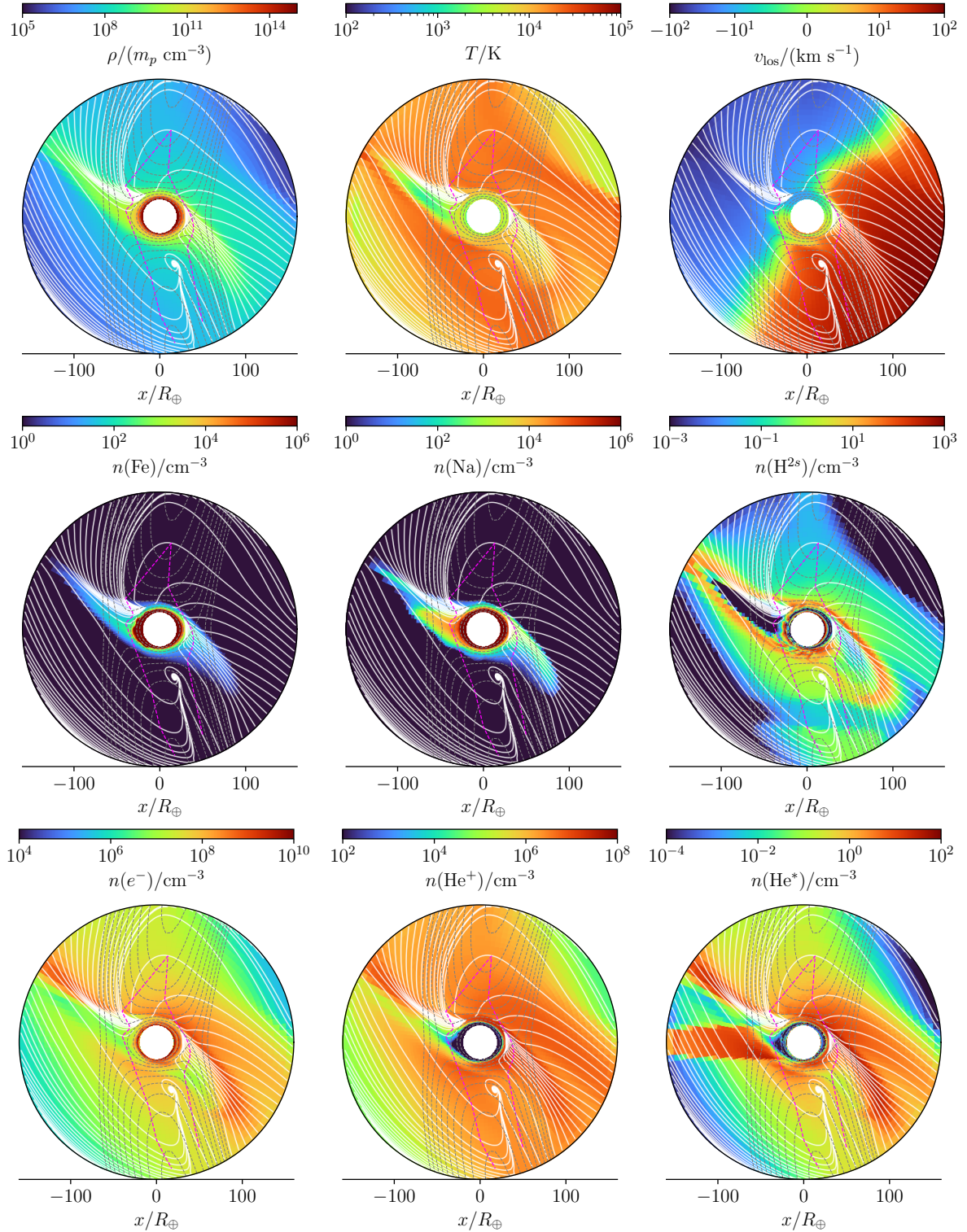


Figure 1. Equatorial slices of key hydrodynamic and thermochemical quantities from the fiducial simulation of WASP-121b. The panels show (from left to right, top to bottom): gas density ρ , temperature T , line-of-sight velocity in the laboratory frame v_{los} , and the number densities of Fe, Na, H^{2s} (metastable neutral hydrogen on the $2s$ state, the $\text{H}\alpha$ absorber), free electrons (e^-), He^+ , and He^* (metastable neutral helium). The snapshot is the temporal average over the final 10 hours over the 300 total simulated hours, after evolving the system through a quasi-steady state (§2.2). The spatial coordinates are in units of Earth radii (R_\oplus), and the central circle marks the nominal planetary radius (R_p). Equipotential contours are shown in gray dotted lines, streamlines are indicated by white lines, and the sonic critical lines are overlaid as dashed magenta lines. The planet orbital motion is downwards, and the host star is to the right.

and settle down with the effective equipotential contours, and then continue the simulations for 200 simulated hours through the final quasi-steady state. To obtain representative conditions for synthetic observations, we time-average all physical quantities over the final 10 simulated hours of each run and perform spectral synthesis on this averaged data.

2.3. Synthetic Observations

To directly compare our simulation results with high-resolution spectroscopic observations, we generate synthetic transmission spectra for selected absorption lines. For a given chemical species X , the wavelength-dependent optical depth τ along a specific line of sight (LoS) at orbital phase Φ is calculated by integrating the contributions from all velocity components along the path:

$$\begin{aligned} \tau(\lambda; \Phi) = & \int_{\text{LoS}} |\text{d}\mathbf{x}| n(X; \mathbf{x}; \Phi) \\ & \times \sum_i \sigma_i[\lambda; \hat{n}_{\text{los}} \cdot \mathbf{v}(\mathbf{x}; \Phi), T(\mathbf{x}; \Phi)] , \end{aligned} \quad (2)$$

where $n(X; \mathbf{x}; \Phi)$ is the number density of the species, and the sum runs over all relevant spectral line components (e.g., the three fine-structure lines of the He * 10830 Å triplet). The cross-section σ_i for each component is modeled as a Voigt profile, accounting for natural broadening, thermal Doppler broadening at the local temperature $T(\mathbf{x})$, and Doppler shifts induced by the projected bulk velocity $\hat{n}_{\text{los}} \cdot \mathbf{v}(\mathbf{x})$ along the LoS.

The relative extinction (i.e., absorption depth) at wavelength λ is then obtained by integrating the attenuated stellar flux over the visible stellar disk:

$$\epsilon(\lambda; \Phi) = 1 - \int \text{d}\Sigma S(\lambda) \exp[-\tau(\lambda; \Phi)] . \quad (3)$$

Here, $S(\lambda)$ is the normalized stellar surface brightness profile, which incorporates limb-darkening and rotational broadening effects appropriate for the host star. This calculation is repeated for multiple LoSs intersecting the planet's atmospheric annulus at each time step during the transit. The resulting collection of $\epsilon(\lambda; \Phi)$ across all phases and LoS constitutes our synthetic transmission spectrum, which can be compared directly to observed data to validate the physical model and interpret kinematic and chemical features.

3. RESULTS: OUTFLOWING ATMOSPHERES AND OBSERVABLES

After evolving the fiducial model for 300 simulated hours through the quasi-steady state, this section presents the principal findings from our fiducial three-dimensional simulation, which models the interactions

between the extended atmosphere of WASP-121b and its host star through radiative transfer and stellar wind forcing. In general, our results reveal that the outer atmospheric structure is dominated by a global, super-sonic outflow that is sculpted by orbital motion and the Coriolis force into two spiral arms, as illustrated in Figures 1 and 2, and explained schematically in Figure 3. The synthetic transmission spectra generated from these simulations demonstrate that specific chemical tracers, each surviving in different atmospheric reservoirs, serve as probes of distinct atmospheric layers and physical processes, from deep circulation to high-altitude dynamics of atmospheric escape.

3.1. Morphology and Dynamics of the Planetary Atmosphere

From both Figure 1 for the equatorial slices and Figure 2 showing the volume rendering, one can clearly identify that the atmospheric dynamics of the model planet is strongly influenced by the host star gravitational field and the orbital motion, which together introduce significant centrifugal and Coriolis forces in the co-rotating reference frame. The planetary interior and lower atmosphere, as traced by the density and chemical species maps, conform closely to the calculated equipotential surfaces, adopting a predominantly ellipsoidal shape elongated toward the host star. This elongation is a direct consequence of the substantial rotational and tidal deformation experienced by the planet in its extremely close-in orbit ($a = 0.026$ AU).

3.1.1. Lower altitudes and atmospheric advection

The equipotential contours overlaid on the hydrodynamic profiles reveal that the Roche lobe, the region where planetary gravity dominates over stellar tidal forces, extends only a few R_{\oplus} beyond the planetary body itself. The characteristic size of this region is given by the Hill radius,

$$\begin{aligned} R_{\text{Hill}} \simeq a & \left(\frac{M_p}{3M_*} \right)^{1/3} \simeq 38R_{\oplus} \times \left(\frac{a}{0.026 \text{ AU}} \right) \\ & \times \left(\frac{M_p}{1.18M_J} \right)^{1/3} \left(\frac{M_*}{1.35M_{\odot}} \right)^{-1/3} . \end{aligned} \quad (4)$$

When compared to the measured planetary radius of $R_p \simeq 21 R_{\oplus}$, the ratio $R_{\text{Hill}}/R_p \lesssim 2$ indicates that the domain of effective planetary gravitational control extends to less than twice the planetary radius from its center. The escape velocity from the planet surface could be estimated as,

$$v_{\text{esc}} \simeq [2GM_p (R_p^{-1} - R_{\text{Hill}}^{-1})]^{-1/2} \simeq 30 \text{ km s}^{-1} . \quad (5)$$

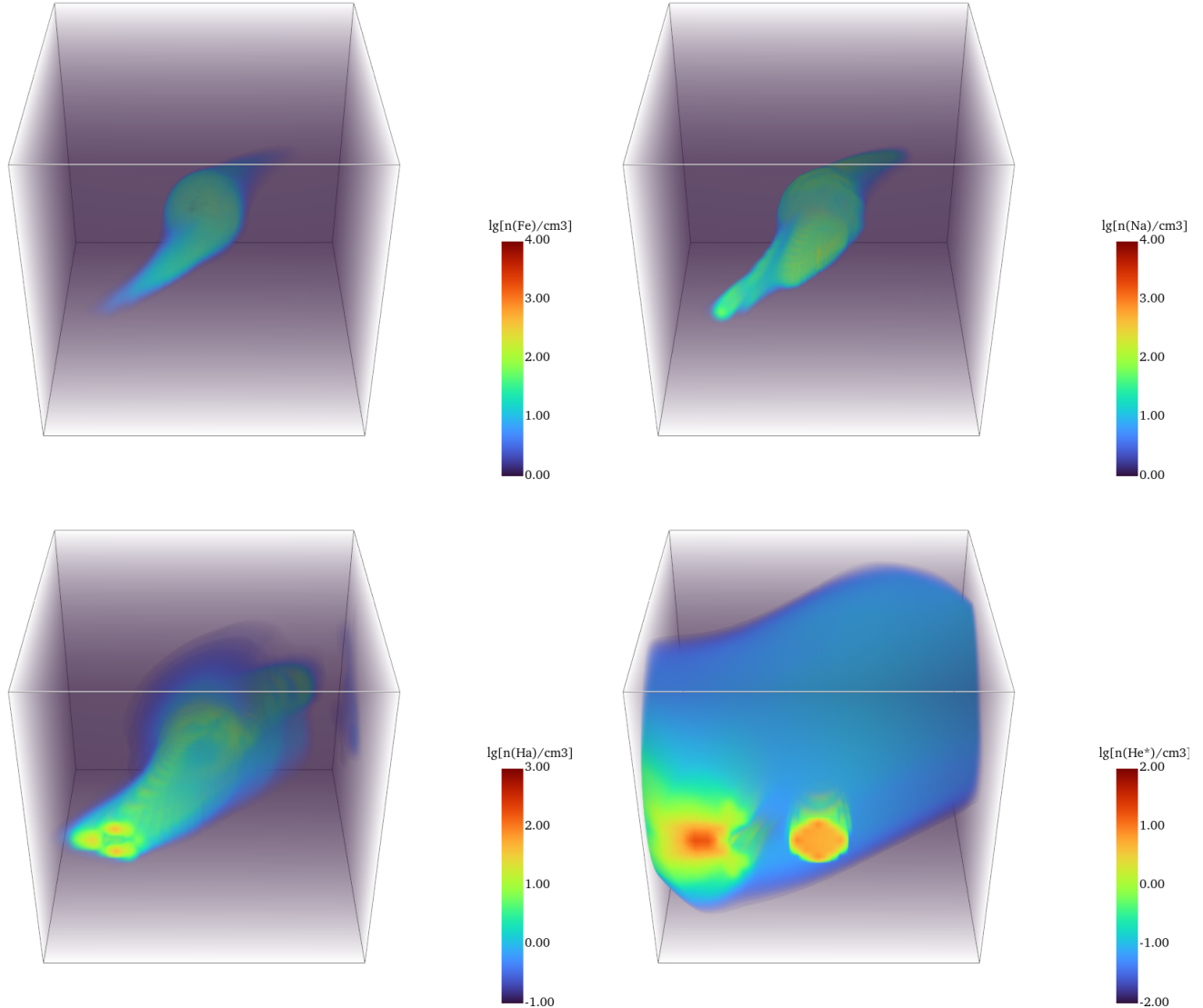


Figure 2. Colormapped volume rendering for the 10-based logarithms of number densities (in cm^{-3}) for four key tracing species (top left: Fe; top right: Na; bottom left: H α ; bottom right: He *). Note that the dynamical ranges of colormaps are different. The host star is on the far side from the reader, and the planet moves from left to right. The rendering boxes have the same sizes ($280 R_{\oplus}$ along every dimension). The high-abundance region of He * in the planet shadow is clearly seen as a cylinder.

Such a relatively low threshold considerably eases the escape of high-velocity streams. Consequently, gaseous material that escapes beyond approximately $1.8 R_p$ undergoes a transition from being primarily bound by the planetary gravity to being governed by orbital kinematics and the stellar gravitational potential.

The hydrodynamic velocity fields presented in Figure 4 illustrate these contrasting flow behaviors across two representative equipotential surfaces. It is noted that the reflecting inner radial boundary condition applied at the planetary surface may not fully capture detailed rotational dynamics or convective motions originating from the deep planetary interior. Therefore,

results pertaining to the innermost atmospheric layers within a few hundred kilometers of the inner boundary should be interpreted primarily in qualitative terms. We also note that the flow patterns are time-dependent and may not converge to a strict steady state over long timescales; the physical quantities shown represent instantaneous snapshots from a dynamically evolving system.

At the lower equipotential surface, located only $\Delta r_0 = 0.1 R_{\oplus}$ above the planetary radius at the substellar point, the flow structure is characterized by a large-scale clockwise anticyclone centered near the substellar longitude, and a counter-clockwise cyclone situated around

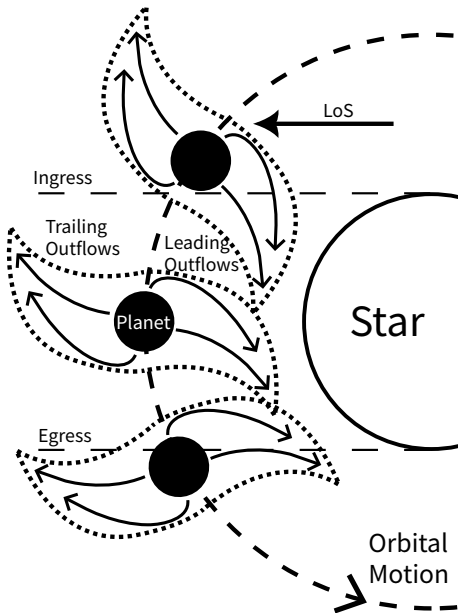


Figure 3. Schematic illustration of the transit geometry and the origin of asymmetric velocity shifts. The planet (black solid circle) moves from top to bottom. The leading (redshifted) and trailing (blueshifted) spiral arms are shaped by both the spilling through the Lagrangian points and the Coriolis force (§3.1). The LoS during ingress and egress samples different projections of the arm velocities, leading to the observed asymmetry in the transmission spectrum.

the antistellar longitude. It is noticed that, although our simulation only covers the northern hemisphere and assumes reflection symmetry across the equatorial plane, the existence and locations of such cyclone and anti-cyclone systems are not qualitatively affected by this simplification, as they cannot exist across the equator (because the directions of rotation are different in the northern versus southern hemispheres). These vortical systems are embedded within broader prograde (west-to-east) zonal winds at the equator, particularly pronounced near the antistellar point where the cyclonic flow itself is prograde. These complex flow patterns arise primarily from day-to-night pressure gradients, which drive gas from the heated dayside toward the cooler nightside. The resulting flow is then deflected by the Coriolis force associated with the planet's tidally locked spin, generating the observed anticyclonic and cyclonic circulations.

At a higher equipotential surface located $\Delta r_0 = 5 R_\oplus$ above the substellar surface, which is still within the planetary Roche lobe but influenced by the expanding outflow, the flow morphology undergoes a notable transition. While residual anticyclonic and cyclonic structures remain visible, the dominant transverse gas motion becomes systematically retrograde (east-to-west).

The significant vertical shear in zonal wind direction, from prograde flow at depth to retrograde motion at higher altitudes, creates conditions conducive to the development of Kelvin-Helmholtz instabilities (KHI). In the fiducial model, this shear layer is most pronounced in the night hemisphere and near the day-night terminators, while still exist in the day hemisphere (see the tangential velocity panels compared in Figure 4). The resulting turbulence can modulate the atmospheric structure on timescales of hours to days, intermittently enhancing or suppressing the local mass flux escaping the planetary potential. Such variations could, in principle, imprint onto time-resolved transmission spectra, and current observations qualitatively imply such variabilities (e.g. [Changeat et al. 2024](#)). Future observations with higher cadences signal-to-noise ratios (SNRs), and spectral resolutions, are required to quantitatively capture these sub-transit variations in detail.

3.1.2. Higher altitudes and outflows

At higher altitudes, the atmospheric dynamics is dominated by outflows. These energetic outflows, driven primarily by XUV irradiation and assisted by optical radiation (see also the analyses in §4) from the host star, eventually organize into the large-scale spiral structures that characterize the extended exosphere. This escaping material organizes into distinct spiral-shaped structures, a morphology reminiscent of (but with gas flow opposite to) the accretion streams observed in the interactions between planets and their residing protoplanetary disks (e.g., [Kley & Nelson 2012](#)).

The formation of the two relatively dense spiral arms is dominated by the interaction of the planetary outflow with the stellar gravitational field and the Coriolis force in the co-rotating frame. On the dayside hemisphere, materials could be heated to spill over the L1 point and accelerated towards the star. Simultaneously, gas flowing from the evening terminator (the boundary between day and night) is deflected by the Coriolis force towards the star, which could also be understood as the local sub-Keplerian motion caused by the planetary orbital speed plus the outflow velocity (opposite to the orbital motion direction). These two sources together shape a dense, leading spiral arm that points toward the host star and with an angular velocity slightly exceeding that of the planet itself. Conversely, on the nightside hemisphere, a trailing arm is formed by analogous processes near the L2 point and the morning terminator. This arm lags behind the planet's orbital motion. The resulting bimodal spiral structure, illustrated in Figure 3, dominates the large-scale morphology of the extended exosphere.

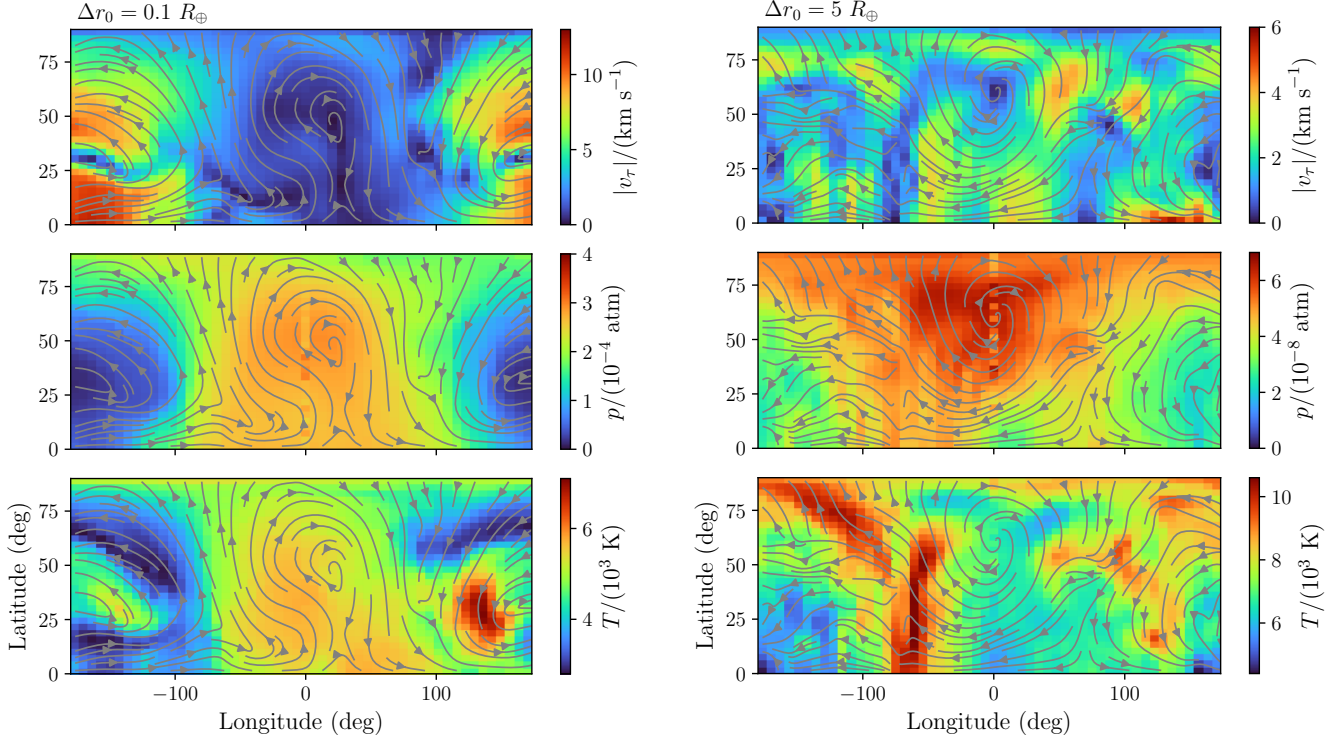


Figure 4. Instantaneous velocity fields in streamlines and arrows, and hydrodynamic quantities in colormaps (tangential wind speed in the top row, pressure in the middle row, and temperature in the bottom row), showing two representative equipotential surfaces from the fiducial simulation. Left column presents the surface near the planetary surface ($\Delta r_0 = 0.1 R_\oplus$ above the substellar radius), illustrating the substellar anticyclone and the antistellar cyclone, along with prograde super-rotation near the equator. Right column presents the equipotential surface at $\Delta r_0 = 5 R_\oplus$, where the retrograde winds are predominantly deflected by the Coriolis force on the outflow.

On the bases of these dense ($\rho \sim 10^{11} m_p \text{ cm}^{-3}$) and relatively cool (close to the equilibrium temperature; $T \sim 3 \times 10^3 \text{ K}$) spiral rams as “spines”, the incident EUV photons further trigger secondary expansion, forming extended arms that are predominantly ionized and heated to $T \sim 3 \times 10^4 \text{ K}$, and attenuated to $\rho \sim 10^8 m_p \text{ cm}^{-3}$. Both the dense and the extended spiral arms are subject to the Coriolis force, inherent to the co-rotating frame of reference, establishes this spiral pattern. Material in the leading arm (advancing ahead of the orbital motion) is deflected outward, resulting in a net redshift in the planetary rest frame when detected, while material in the trailing arm produces a corresponding blueshift. We note that the planetary spin, assumed to be tidally locked, does not exert a significant influence on the large-scale outflow dynamics at altitudes several Earth radii above the inner boundary, at least in the absence of strong magnetic coupling.

As indicated by the velocity streamlines, the dense spiral-arm features originate mainly by in the vicinity of the L1 and L2 Lagrangian points, when the heated atmosphere at lower altitudes fills up the Roche lobe, spilling out, and guided by the morphologies of equipo-

tential surfaces. The gas inside dense spiral arms undergoes acceleration from near-stagnation conditions at the base to transonic velocities near the Lagrangian points. The divergent streamlines of the flow above these points form nozzle-like conditions that further accelerate the outflow to supersonic velocities, enabling escape from the planet gravitational potential.

3.2. Thermochemical Conditions and Detectables

Observational insights into the kinematics and thermochemistry are obtained by linking synthetic spectra to the underlying thermochemical species distributions in the simulation. As illustrated in Figures 1 and 2, the four primary spectroscopic tracers (neutral sodium Na, neutral iron Fe, H α , and metastable helium He *) exhibit distinct spatial distributions that reflect their differing population mechanisms and vulnerability to photoionization and collisional ionization. Note that neutral iron has numerous absorption lines, and we select one representative line at $\lambda = 4490 \text{ \AA}$ for kinematic analysis, which adequately captures the gas motions revealed by iron features. For sodium, the two D lines are separated

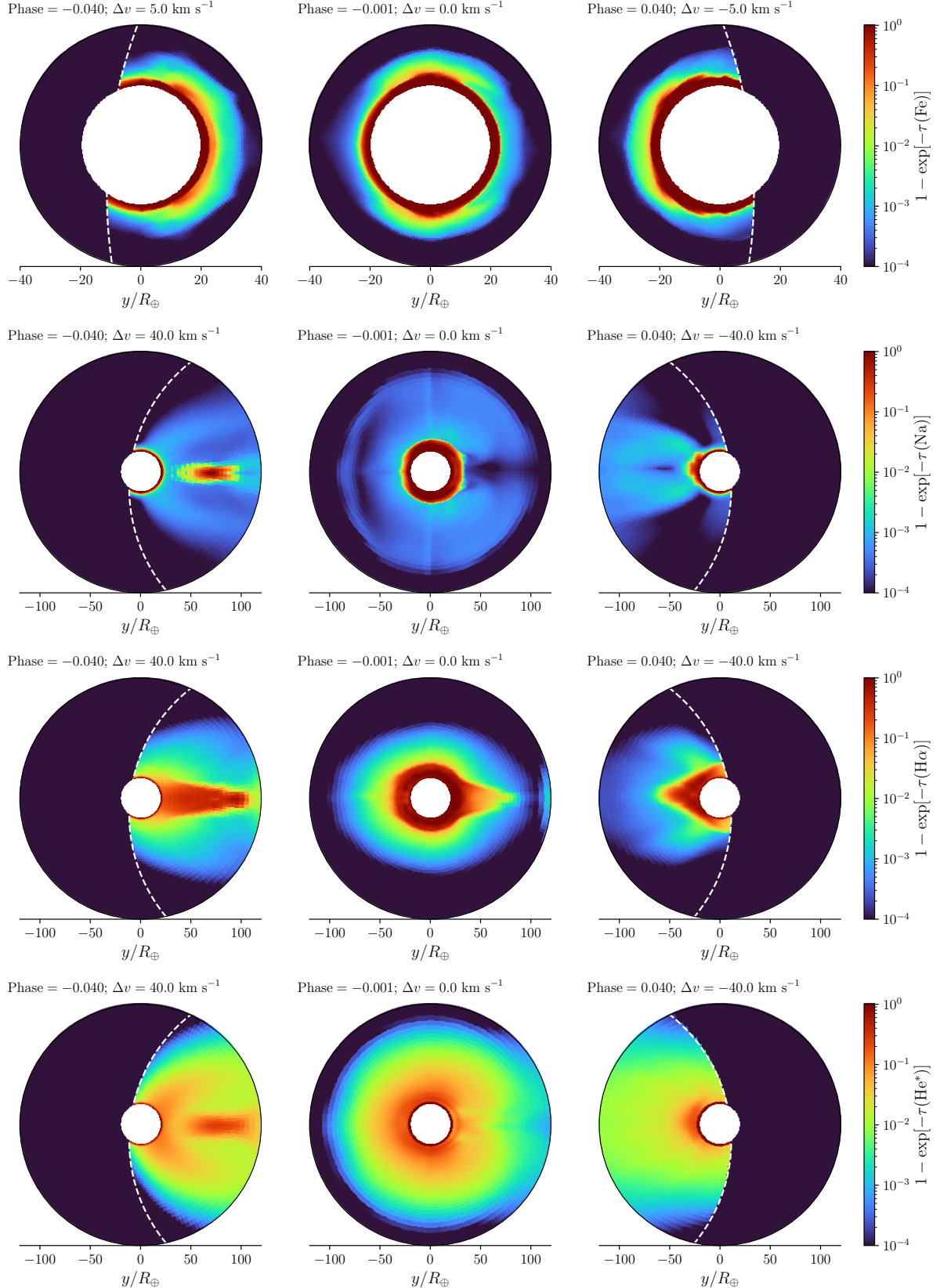


Figure 5. Extinction intensities (quantified by $1 - e^{-\tau}$) at three different velocities and orbit phases (denoted at the top of each panel) for four key tracers from the fiducial simulation (denoted at the colorbar in each row). White dashed circles indicate the projection of the host star, in which the extinction by planetary atmospheres are calculated. The asymmetric velocity shifts and phase-dependent absorption depths trace the geometry and kinematics of the spiral arms and inner atmospheric layers.

by ~ 6 Å (equivalent to ~ 300 km s $^{-1}$); we consider only the 5896 Å line as representative.

Our simulations identify four principal reservoirs where these species can survive the intense stellar irradiation:

1. The high-density interior region: Inside the planetary photosphere, extreme column densities shield neutral species from high-energy photons.
2. The planet shadow: The region directly behind the planet receives no direct stellar illumination, maintaining relatively cool, neutral conditions.
3. The dense spiral arms: Gas densities reaching $\rho \gtrsim 10^{11} m_p$ cm $^{-3}$ create optically thick barriers that attenuate EUV radiation, while allowing deeper-penetrating X-ray and FUV photons to reach regions closer to the planetary surface.
4. The extended spiral arm structures: The diffuse outer parts of the arms, heated by EUV and soft X-ray irradiation. The ionized fraction here is higher than in the first three reservoirs but still not fully ionized. This region favors neutral species that require some ionization for excitation (e.g., He *).

These distinct reservoirs create chemically stratified layers with different observational consequences. The synthetic transmission spectra illustrated in Figure 6 exhibit reasonable, qualitative to semi-quantitative agreement of velocity shifts and amplitudes (due to the uncertainties of the actual abundances of metals near the planet photosphere) with Seidel et al. (2025). The observable signatures of different chemical species indicate different physical mechanisms and processes.

3.2.1. Fe and inner regions

As one can confirm by inspecting Figures 2 and 5, Fe primarily tracks the kinematics of the inner layer, primarily revealing the motion from dayside to the nightside. When superposed with the rotation of the frame (originating from the tidally locked spin), whose linear speed satisfies,

$$v_{\text{rot}} = \left(\frac{GM_*}{a^3} \right)^{1/2} R_p = 6.9 \text{ km s}^{-1} \times \left(\frac{a}{0.026 \text{ AU}} \right)^{-3/2} \left(\frac{R_p}{20R_{\oplus}} \right)^{-3/2}, \quad (6)$$

the velocity signal identified by Fe becomes slightly redshifted at ingress and systematically blueshifted

throughout the rest of the transit. In the time-dependent transmission spectra, Fe absorption profiles exhibit the characteristic tidally locked spin signature (redshift at ingress, blueshift at egress), superposed with a systematic blueshift of ~ 3.5 km s $^{-1}$ that traces day-night circulation patterns. This is in quantitative agreement with the results of Seidel et al. (2025), comparing the observation errorbars and the excess absorption colormap illustrated in Figure 6.

3.2.2. Na and the dense spiral arms

At altitudes higher than where neutral Fe survives, velocities are also influenced by orbital motion. The spatial distribution of Na that contributes to the transmission spectra can be divided into the dense reservoirs near the planet and the spiral arms, the latter of which exhibits relatively large velocities (see also Figure 5). One prospective curiosity is how neutral Na survives the intense FUV radiation (especially in the 6 eV band with intense photon flux), which can penetrate the dense spiral arms almost unattenuated. At the peak band intensity $F(6 \text{ eV}) = 2 \times 10^{18} \text{ cm}^{-2} \text{ s}^{-1}$, the photoionization rate of Na is $\zeta(\text{Na}) \simeq 3 \times 10^{-3} \text{ s}^{-1}$. Meanwhile, the recombination timescale in the spiral arms is approximately

$$\begin{aligned} \tau_{\text{rec}}(\text{Na}) &\equiv \frac{n(\text{Na})}{\alpha_{\text{Na}} n(\text{Na}^+) n_e} \\ &\simeq 3 \times 10^2 \text{ s} \times \left(\frac{T}{10^4 \text{ K}} \right)^{0.68} \left(\frac{n_e}{10^8 \text{ cm}^{-3}} \right)^{-1} \\ &\quad \times \left[\frac{n(\text{Na}^+)}{10^4 \text{ cm}^{-3}} \right]^{-1} \left[\frac{n(\text{Na})}{10^2 \text{ cm}^{-3}} \right], \end{aligned} \quad (7)$$

using the recombination rate from McElroy et al. (2013) (also implemented in our simulations). As $\tau_{\text{rec}}(\text{Na}) \sim 1/\zeta(\text{Na})$, recombination can offset ionization and maintain a significant neutral sodium fraction in the spiral arms (see also Figure 7). The velocity magnitudes within the spirals, estimated from stellar potential acceleration Δv_r and Coriolis deflection Δv_{co} (where Δr is the distance traveled after leaving the Roche lobe),

$$\begin{aligned} |\Delta v_r| &\sim \left(\frac{GM_*}{2a^2} \Delta r \right)^{1/2} \sim 40 \text{ km s}^{-1} \times \left(\frac{\Delta r}{2R_p} \right)^{1/2}, \\ |\Delta v_{\text{co}}| &\sim 2\Omega\Delta r \sim 30 \text{ km s}^{-1} \times \left(\frac{\Delta r}{2R_p} \right), \end{aligned} \quad (8)$$

are of order ~ 30 km s $^{-1}$ at $\sim 2R_p$ from the planetary surface. Although these velocities could increase at larger distances, the observed velocity shifts in secondary Na excess absorption are limited to $|\Delta v| \lesssim$

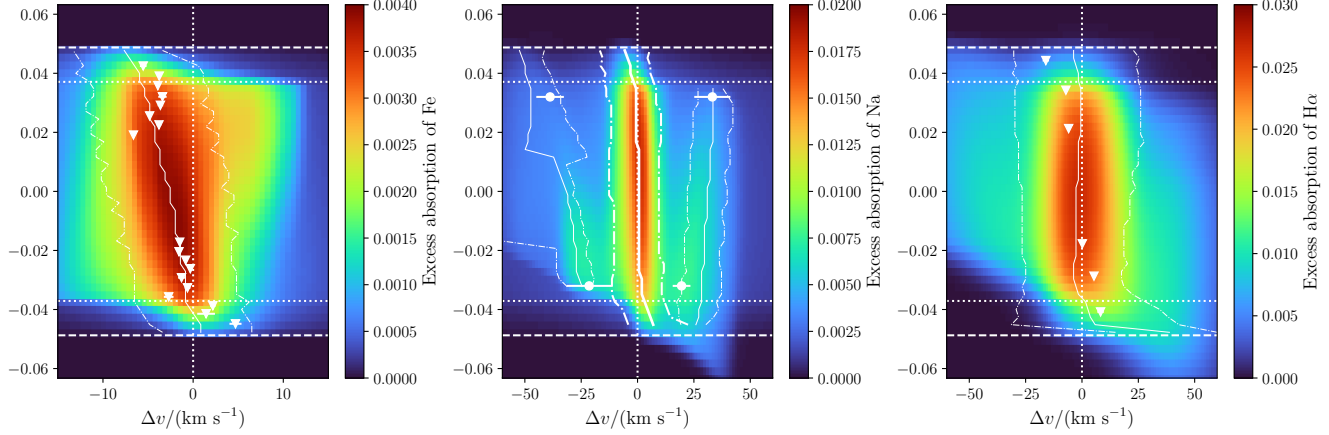


Figure 6. Absorption spectra of Fe (left panel), Na (middle panel), and H α (right panel), illustrated as excess absorption at different velocities (horizontal axes) and orbital phases (vertical axes). Horizontal white dashed lines indicate the starts of ingress and the ends of egress, and horizontal white dotted lines indicate the ends of ingress and starts of egress. The vertical dotted lines indicate zero velocity shifts for reference. The absorption peaks, evolving with orbital phases, are tracked with solid lines for the centroids, and the dash-dotted lines for the half-maximum widths. For the Na panel, the central peak are tracked by heavy solid and dash-dotted lines. Errorbars for Fe and H α indicate the fitting results and uncertainties (not widths) reported by Seidel et al. (2025). More detailed comparison of H α spectra is shown in Fig. 9 and discussed in §3.2.3. The errorbars for the Na panel indicate the fitting centroids and widths within this work (by using the observation transmission data presented in Seidel et al. 2025). More detailed comparisons of Na spectra are shown in Fig. 8 and Fig. 12. These results are discussed in §3.2.2 and §4. Observation errorbars are shifted to the red side by 3 km s $^{-1}$ for better fitting of the trend (note that the observed velocity shifts may not have a fixed calibration).

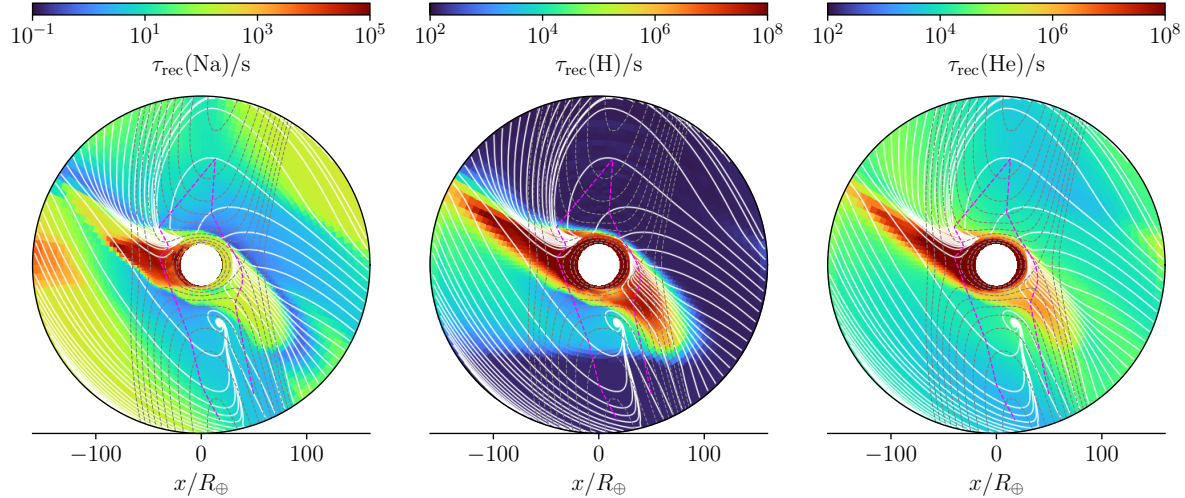


Figure 7. Recombination timescales of Na (left panel), H (middle panel, to the 2s level, from H $^+$ via the recombination with e $^-$ and charge exchange with neutral H), and He (right panel; to the metastable state, via the recombination from He $^+$).

50 km s $^{-1}$ (see also Seidel et al. 2025). This observational constraint implies that the Na-rich spiral arm material must be confined to regions relatively close to the planet, typically within $\lesssim 5 R_p$. Our simulations indicate that this confinement is enforced by the intense FUV flux from the F6V host star WASP-121, which limits the survival of neutral sodium to these inner regions. Geometric effects during the transit further modulate the observed velocity shifts. During ingress, the lead-

ing spiral arm presents a larger spatial extent but a smaller LoS velocity component because its motion is primarily perpendicular to the LoS. Conversely, during egress, the trailing arm presents a more favorable geometry for observing Doppler shifts (see Figure 3). As a result, the velocity shift immediately after ingress is $\Delta v \simeq 20$ km s $^{-1}$, considerably smaller than the blueshift magnitude on the egress side ($|\Delta v| \simeq 35$ km s $^{-1}$).

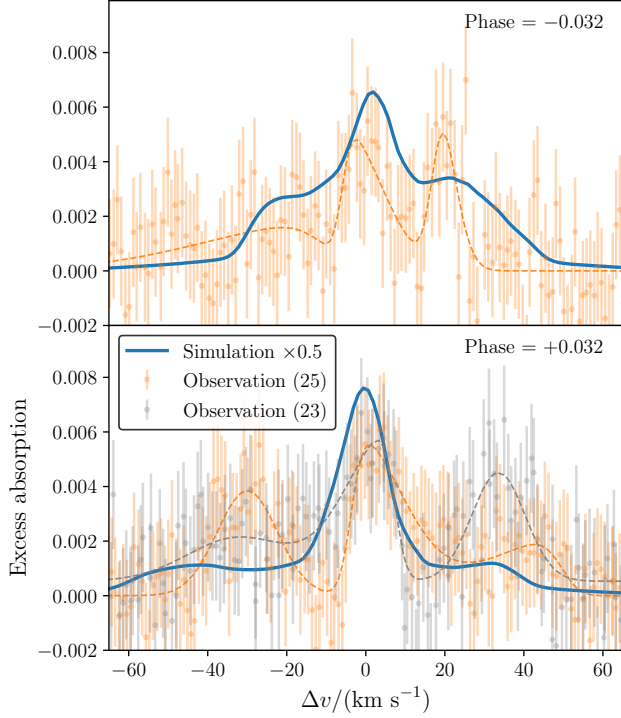


Figure 8. Comparisons of excess absorption of Na, between the fiducial simulation results (in solid blue lines; multiplied by a factor of 0.5, see §3.2), the observations indicated with errorbars in Seidel et al. (2023) [grey errorbars, egress only, marked as “Observation (23)”] and Seidel et al. (2025) [orange errorbars, both ingress and egress, marked as “Observation (25)”], and the fitting results within this work (using the errorbar data, presented in dashed lines in the same color as the corresponding errorbars).

Comparison between our simulated transmission spectra and observations from the morning (ingress) and evening (egress) limbs (Fig. 8) shows semi-quantitative agreement, though the model amplitudes have been scaled down by a factor of 0.5 to match the data. This scaling is consistent with uncertainties in the planetary sodium abundance, which is known to be substellar for WASP-121b (Seidel et al. 2023).

A detailed inspection of the observed transmission spectra reveals intriguing asymmetries not fully captured by previous atmospheric models. During ingress, a relatively obscured but marginally detectable blueshifted absorption component appears alongside the dominant redshifted secondary peak. Conversely, during egress, a noticeable redshifted tertiary feature coexists with the primary blueshifted absorption.

These “tertiary” peaks, not fully reproduced in existing spectral retrievals (Seidel et al. 2025), are difficult to reconcile with a uniform prograde super-rotating jet,

which would generate largely symmetric morning and evening signatures.

Moreover, the velocity separation between the secondary and tertiary absorption features differs between the morning and evening limbs, indicating a distinct morning-evening asymmetry in atmospheric kinematics. The 3D spiral-arm model could account for these complex spectral features. While the leading spiral arm dominates absorption on the morning limb, the trailing arm also contributes with oppositely directed velocity shifts due to Coriolis deflection. Additionally, geometric projection effects cause the spiral arms to appear more spatially extended but less velocity-broadened during ingress (when they are more perpendicular to the line of sight), with the reverse occurring during egress (see Fig. 3). We also notice that the amplitudes and velocity separations of the secondary and tertiary peaks show variability between the observational datasets of Seidel et al. (2023) and Seidel et al. (2025). Such variability is consistent with intrinsic hydrodynamic instabilities in the atmospheric outflow (see the KHI discussion in §3.1.1). Therefore, our spiral-arm model provides a complimentary explanation for the observed Na line profiles without requiring extreme near-surface jet streams with velocities comparable to the planetary escape velocity (equation 5).

3.2.3. H α and metastable helium in the extended arms

The H α transmission spectral profiles, as shown in Figures 1 and 2, originate from extended regions predominantly located outside the planetary Roche lobe. These regions are dynamically coupled to orbital motion and stellar gravity rather than to the planet spin. The lower level of the H α transition, H 2s , is populated primarily via recombination of H $^+$ and charge exchange between H and H $^+$, processes that are significantly faster than direct collisional pumping. The timescale for collisional excitation to the 2s state (the excitation to the 2p state would instead lead to instant Ly α emission) is approximately,

$$\begin{aligned} \tau_{\text{coll}}(\text{H}^{2s}) &\equiv \frac{1}{k_{1s \rightarrow 2s} n_e} \\ &\sim 1 \text{ s} \times \exp\left(\frac{118400 \text{ K}}{T}\right) \left(\frac{T}{10^4 \text{ K}}\right)^{-0.455}, \end{aligned} \quad (9)$$

based on data from Christie et al. (2013) and Janev et al. (2003). This timescale increases to $\tau_{\text{coll}} \sim 10^5$ s at $T = 10^4$ K near the interface of the dense to extended spiral arms, and to $\tau_{\text{coll}} \sim 2 \times 10^{10}$ s at $T = 5000$ K within the denser arms, making recombination and charge exchange the dominant population mechanisms (middle panel of Figure 7). Consequently, H 2s

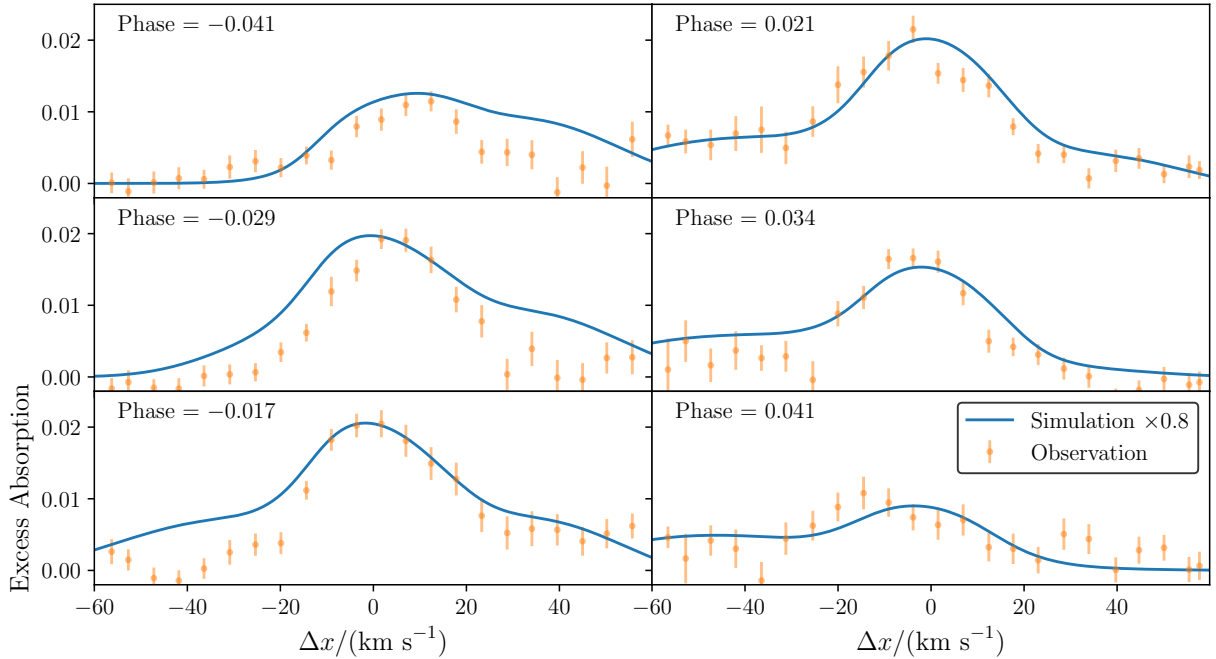


Figure 9. Comparing the simulated transmission spectra of H α (blue solid lines; multiplied by a factor of 0.8) to the observations (orange errorbars; from Seidel et al. 2025) at different orbital phases, near the ingress (left column) and egress (right column), respectively. Note the secondary peaks, redshifted at Phase < 0 (near ingress), and blueshifted at Phase > 0 (near egress).

(the 2s state of neutral hydrogen responsible for H α absorption) resides in regions with a relatively high ionization fraction, specifically tracing the interface between the dense spiral arms and the EUV-irradiated extended arms where hydrogen is nearly fully ionized.

Comparison of the simulated transmission spectra with observations (Figure 6) shows that the orbital phase dependence of the peak velocity generally matches the observed trend. Notably, both the simulations and the data reveal secondary absorption peaks at velocities $|\Delta v| \gtrsim 40 \text{ km s}^{-1}$ for H α , features that were not explicitly identified by Seidel et al. (2025). Similar to neutral Na, these secondary peaks arise because the interface between the dense and extended spiral arms extends to distances $\gtrsim 10^2 R_{\oplus}$ from the planet, where gas is accelerated to $\sim 40 \text{ km s}^{-1}$ by the stellar gravitational potential and Coriolis force (eq. 8).

Figure 9 demonstrates a good agreement in both the central and secondary high-velocity peaks across multiple orbital phases, although the simulated amplitudes have been scaled by a factor of 0.8 to account for uncertainties in the stellar EUV luminosity and in the atomic rate coefficients for recombination to the 2s level and collisional transfer to the 2p level. We note that using alternative collisional rate data (e.g., from Osterbrock & Ferland 2006) could suppress the H α absorption amplitude by a factor of ~ 40 . These secondary peaks could

be overlooked in previous analyses that did not account for spiral arm structures.

Similarly, metastable helium (He *) absorption arises in regions where recombination populates the metastable triplet ground state of helium (right panel of Figure 7). The He * absorbers are spatially more extended than those of H α , though their number density is considerably lower. Since He * is efficiently destroyed by photoionization from photons above 4.8 eV, a prominent shadow tail forms behind the planet (see Figure 2), a feature previously identified in studies of evaporating exoplanets (e.g., Wang & Dai 2021a,b). Due to the finite extent of our simulation domain, we cannot compare the equivalent width of the He 10830 Å line over the entire orbital period with observations. At least, the dimensionless equivalent width in the $10830 < (\lambda/\text{\AA}) < 10840$ band defined as (F_c for the unabsorbed continuum component of the spectrum, and F_{λ} for the spectrum with absorption; $\Delta\lambda = 10 \text{ \AA}$),

$$[W/\Delta\lambda](\text{He}) \equiv \frac{1}{\Delta\lambda} \int_{10830 \text{ \AA}}^{10830 \text{ \AA} + \Delta\lambda} d\lambda \frac{F_c - F_{\lambda}}{F_c \Delta\lambda}, \quad (10)$$

is obtained from our simulation $[W/\Delta\lambda](\text{He}) \sim 3600 \text{ ppm}$ at mid-transit, agrees quantitatively with the values reported by Czesla et al. (2024); Allart et al. (2025) when accounting for the fact that the observed in-transit absorption is an average over the full tran-

sit, which tends to yield a shallower absorption depth (~ 2800 ppm) than the mid-transit value.

4. PARAMETRIC STUDY

While the fiducial model provides a baseline understanding, the interactions of physical processes governing atmospheric escape necessitates a broader exploration of the parameter space. To systematically quantify the sensitivity of our results and identify the dominant physics shaping the observables, we conducted a series of controlled numerical experiments summarized in Table 2, mainly experimenting the impacts of the stellar radiation and winds. These simulations are also illustrated in Figures 10 and 11, showing especially the profiles of Na which traces the most prominent spiral arm features.

4.1. Dependence on High-Energy Radiation Flux

The spectral energy distribution of the host star plays a dual role, by providing the energy that drives atmospheric escape, but also ionizes and dissociates the very atomic and molecular species used to trace the outflow. Our simulations examine how different energy bands distinctly shape the observable properties of the escaping atmosphere, with each band influencing the outflow density, velocity, and chemical composition in different ways.

Model FUV10 (which has an FUV flux enhanced by a factor of 10 relative to the Model 0) demonstrates that FUV radiation primarily controls the abundance and distribution of tracer species via photoionization and launching outflows. FUV photons with energies above 4.8 eV can photoionize metastable helium, while those above 5.14 eV ionize neutral sodium. In Model FUV10, the stronger FUV field leads to a more vigorous outflow, while the resulting higher densities in the spiral arms help maintain a relatively abundant population of neutral Na via recombination (although with much stronger photoionization) out to larger distances from the planet despite the enhanced photoionization rate (see Figure 10, row FUV10). Stronger outflows make the secondary and tertiary peaks in the morning-evening Na transmission spectra significantly more prominent, and move them further away from the $\Delta v = 0$ center as they travel and get accelerated farther from the planet (see also Figure 12). As the Na secondary peaks appear to be less prominent than the observed data in the fiducial model, it is possible that the real values of FUV fluxes stays somewhere between Models 0 and FUV10. Conversely, a simulation with an FUV field reduced to one-tenth of the fiducial value (not shown in this paper) yields much less dense spiral arms, exhibiting a narrower

spatial and velocity extent of Na absorption, as well as a smaller equivalent width of the He 10830 Å line. We note, however, that such a weak-FUV scenario is astrophysically unlikely for a star like WASP-121, whose FUV flux originates primarily from the stellar blackbody component.

In the current Model 0, which lacks solid grains (presumed to be fully sublimated at the high temperatures of ~ 2400 K), one of the main opacity sources is H⁻, which is susceptible to photoionization by optical radiation (represented by the $h\nu = 2$ eV band). However, because the regions where H⁻ absorbs optical photons are deep within the gravitational potential well (near the planetary surface), Model OPT3 (with optical flux enhanced by a factor of 3) launches the outflow at a rate only slightly stronger than the fiducial model (approximately $1.3\times$ the mass-loss rate). This model also produces an excess Na absorption peak on the ingress side that extends to a redshift velocity of ~ 40 km s⁻¹. Similarly, Model DUST, which assumes a higher abundance of sub-micron refractory carbonaceous grains (graphites, or polycyclic aromatic hydrocarbons, PAHs, which can survive at much higher temperatures than silicate grains; see also Xu et al. 2026) as an additional opacity source, enhances the atmospheric mass-loss rate to even higher than OPT3. These grains efficiently absorb stellar radiation and transfer energy to the gas, effectively increasing the heating efficiency in the lower atmosphere. Both Models OPT3 and DUST exhibit synthetic Na absorption features that appear closer to the observation than the fiducial Model 0, in terms of secondary and tertiary peak locations and amplitudes (Figure 12), yet more deterministic conclusions could only be addressed with future observations with higher spectral SNRs.

Model XR10, with enhanced X-ray flux, produces Fe, and H α absorption features very similar to those of the fiducial Model 0. Notably, the Na absorption feature is more consistent with observations compared to the fiducial model (Figures 11 and 12). However, the equivalent width of the metastable He absorption line is approximately ~ 5 times stronger than the observed value. Apart from these tracers, X-ray photons could potentially drive significant changes in the deeper atmospheric layers, a topic we leave for future investigations. Model EUV10, with enhanced extreme ultraviolet flux, launches a much broader set of “extended spiral arms” on top of the depleted dense spiral arms, making the spiral structures more diffuse and extended. Meanwhile, the neutral species in these arms are effectively destroyed by the unattenuated FUV and EUV radiation. Because the recombination rate of ions like Na⁺

Table 2. Various models based on the fiducial model for WASP-121b

Model Code	Description	$\dot{M}/(10^{-7} M_{\oplus} \text{ yr}^{-1})$	$[W/\Delta\lambda](\text{He})^{\dagger}/10^{-3}$
0	Fiducial Model (§3)	0.64	3.6
OPT3	$3\times$ flux at $h\nu = 2 \text{ eV}$.	0.75	3.5
FUV10	$10\times$ fluxes at $(h\nu/\text{eV}) \in \{4.9, 6, 12\}$	11.8	1.5
EUV10	$10\times$ fluxes at $(h\nu/\text{eV}) \in \{20, 60\}$	1.17	23.9
XR10	$10\times$ fluxes at $(h\nu/\text{keV}) \in \{0.3, 3\}$	4.5	18.4
DUST	$n(\text{Gr})/n_{\text{H}} = 10^{-9}$	0.96	3.3
WIND	$\dot{M}_{\text{wind}} = 6 \times 10^{-12} M_{\odot} \text{ yr}^{-1}$	0.26	10.9

NOTE— \dagger : $[W/\Delta\lambda]$ is the dimensionless equivalent width of He 10830 Å absorption line in the wavelength band $10830 < (\lambda/\text{\AA}) < 10840$ (equivalent to the absorbed fraction in the same band) at the mid-transit (see eq. 10).

scales roughly with the square of the gas density, the low-density extended spiral arms cannot maintain a sufficient population of neutral Na atoms, leading to a suppression of both the spatial and velocity extent of the Na absorption features. At the same time, the stronger EUV flux significantly enhances metastable helium absorption by ionizing more helium, which then recombines more efficiently, increasing the equivalent width of the He 10830 Å line by an order of magnitude relative to the observed value.

4.2. Dependence on Stellar Wind Properties

The fiducial Model 0 assumes no impinging stellar wind. A test run with a weak stellar wind (mass-loss rate $\dot{M}_{\text{wind}} = 10^{-14} M_{\odot} \text{ yr}^{-1}$; not shown in this paper) also yields observational results nearly identical to the fiducial case. This consistency aligns with the observed persistence of He* absorption over extended time periods, as a stronger wind would otherwise disrupt or remove the extended spiral arms from the planet's vicinity, thereby spatially truncating the He 10830 Å absorption features.

Although unlikely to exist for such a F6V star as WASP-121, a much stronger stellar wind could interact dynamically with the planetary outflow via a contact discontinuity, exerting a ram pressure that can confine, compress, and reshape the escaping atmosphere. Model WIND explores this scenario with a substantially enhanced stellar wind (mass-loss rate $\dot{M}_{\text{wind}} = 6 \times 10^{-12} M_{\odot} \text{ yr}^{-1}$ at 400 km s^{-1} radial speed, plus a 200 km s^{-1} orbital motion component). The increased ram pressure effectively confines the planetary outflow on the dayside, compressing it into a narrower structure, while leaving the nightside outflow and spiral arms relatively intact (Figure 11, row WIND). This dayside confinement yields generally similar velocity structures in the excess absorption features of Fe, Na, and H α

compared to the fiducial model. The amplitude of the Na absorption during ingress becomes slightly stronger due to the higher gas density in the compressed region, which enhances recombination rates and thus maintains a higher neutral sodium fraction against FUV photoionization.

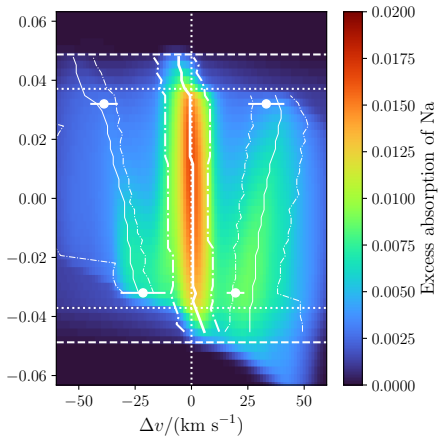
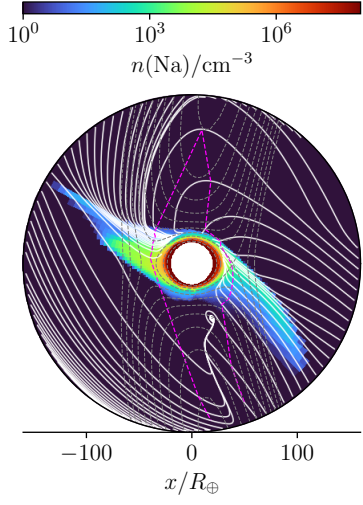
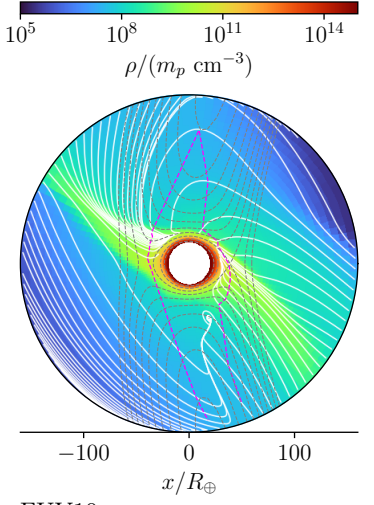
Notably, the equivalent width of the He 10830 Å absorption line at mid-transit is drastically enhanced in the Model WIND. The wind-induced compression increases the density at the interface between the dense spiral arm and the more extended outflow, thereby boosting the rate of He $^+$ recombination into the metastable triplet state He*. Consequently, metastable helium absorption serves not only as a tracer of the escaping atmosphere but also as a sensitive indicator of wind-planet interactions, analogous to the diagnostic role proposed in earlier studies of evaporating exoplanets (Wang & Dai 2021a,b).

5. DISCUSSION AND SUMMARY

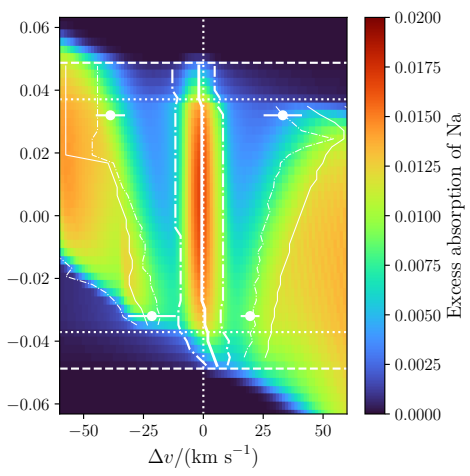
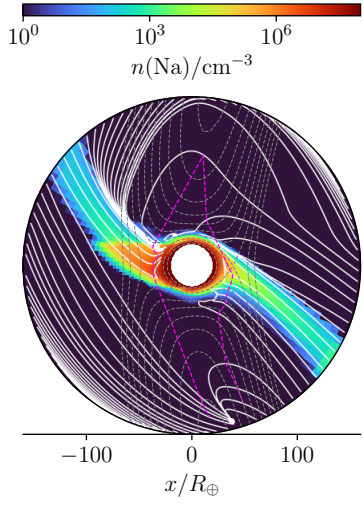
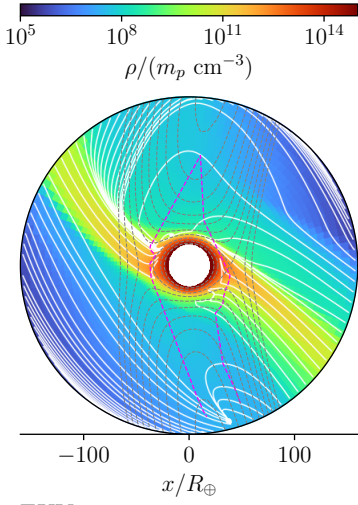
This study presents a new series of three-dimensional hydrodynamic simulations of the ultra-hot Jupiter WASP-121b, which are self-consistently co-evolved with ray-tracing radiative transfer and non-equilibrium thermochemistry. By utilizing the GPU-accelerated Kratos framework, our simulations span from the inner atmospheric circulation regions near the planetary surface out to the extended, escaping exosphere, thereby overcoming the limitations of altitude ranges inherent in most GCM simulations.

The fiducial simulation reveals that the inner atmospheric kinematics are characterized by day-to-night circulation patterns modulated by the planet's tidally locked spin, featuring prominent anticyclonic flow on the dayside and cyclonic structures on the nightside. At higher altitudes, the atmospheric structure is dominated by a supersonic photoevaporative outflow, which

OPT3



FUV10



EUV10

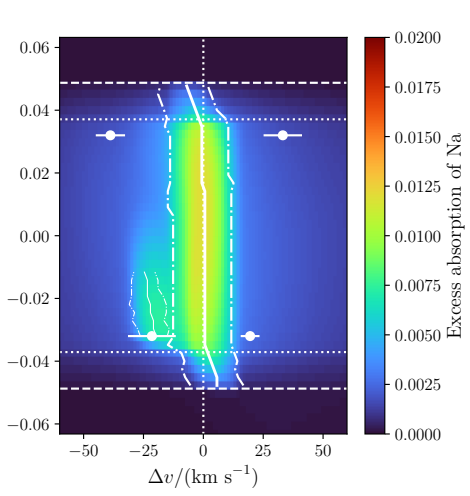
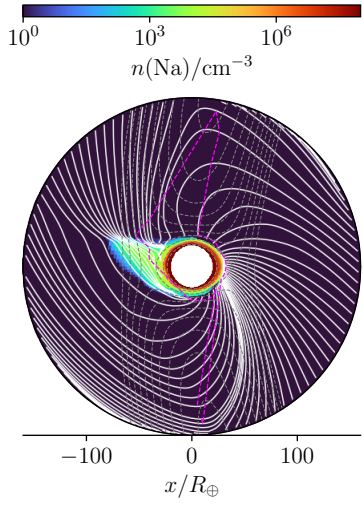
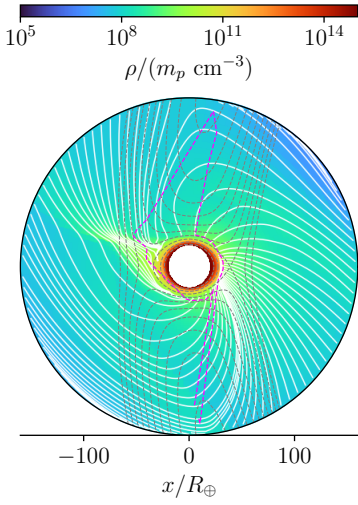


Figure 10. Multiple models (OPT3, FUV10, and EUV10; marked on the top-left of each row) exploring the responses to physical parameters of the planetary outflows (§4 and Table 2), showing the mass density (left column) and neutral Na (middle column) in the equatorial plane (similar to Figure 1), as well as the excess absorption spectra by Na (similar to Figure 6).

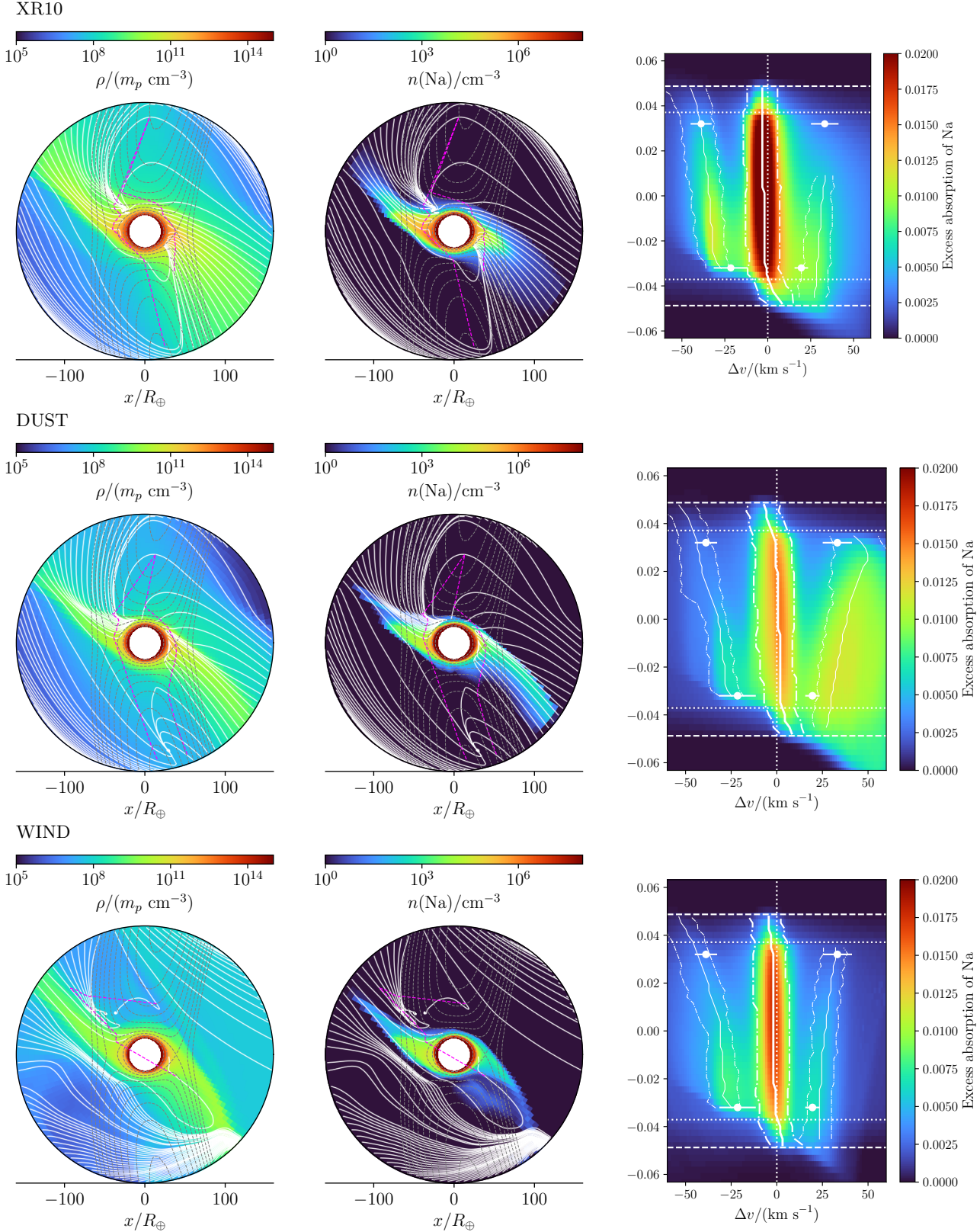
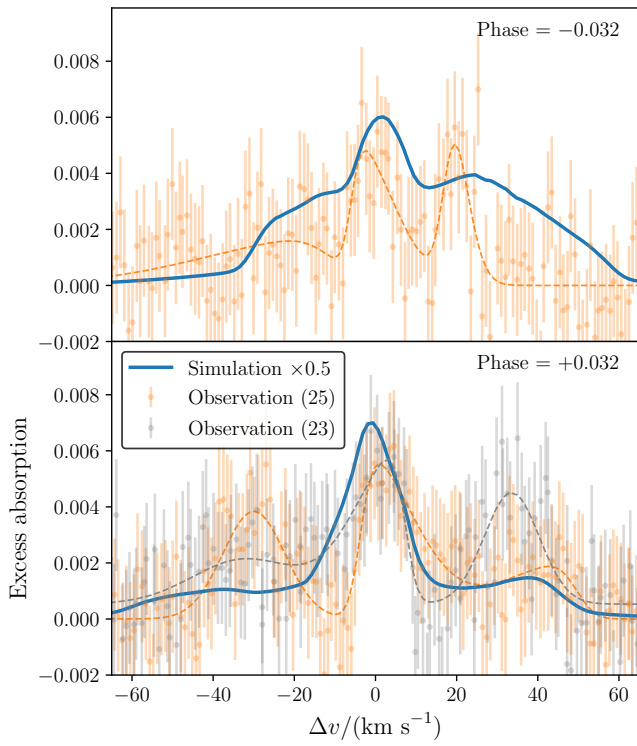
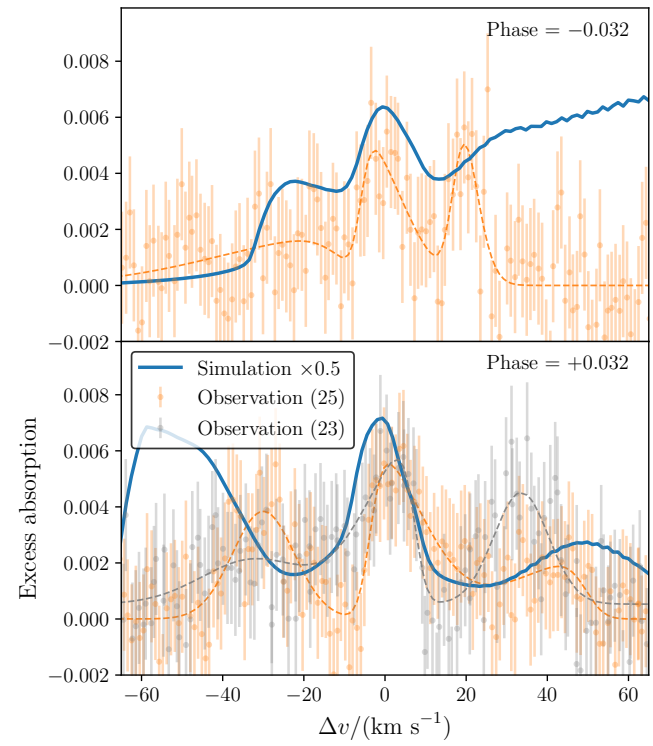


Figure 11. Similar to Figure 10, for models XR10, DUST, and WIND.

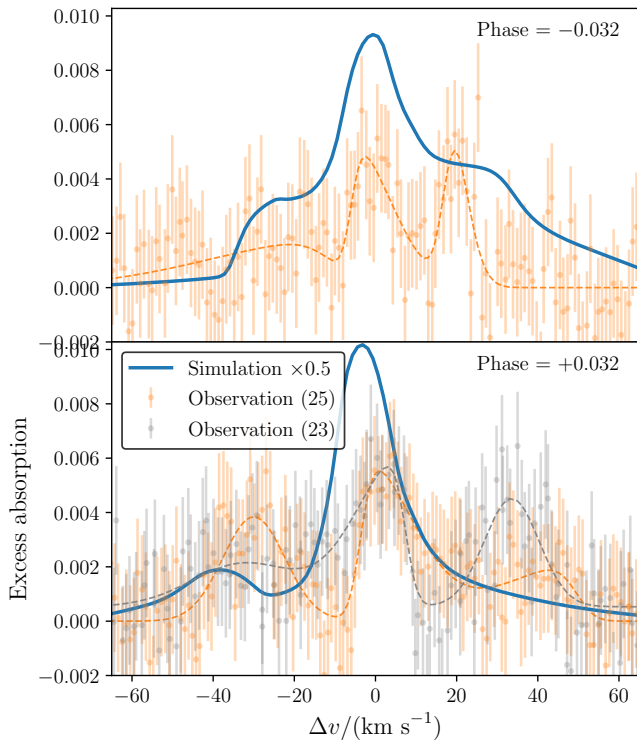
OPT3



FUV10



XR10



DUST

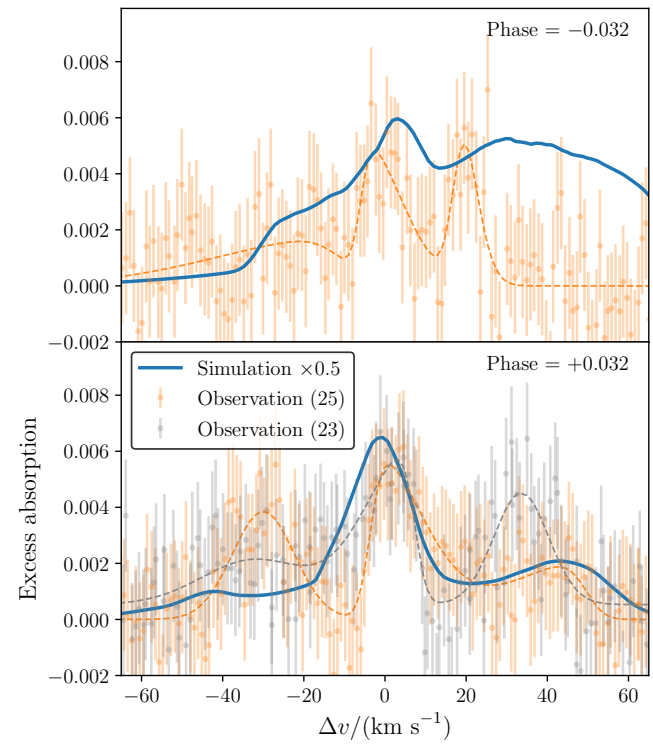


Figure 12. Similar to Figure 8, but for Models OPT3 (upper left), FUV10 (upper right), XR10 (lower left), and DUST (lower right).

is shaped by the combined effects of orbital motion, stellar gravity, and the Coriolis force into two distinct, relatively dense spiral arms with gas densities $\rho \gtrsim 10^{10} m_p \text{ cm}^{-3}$. These dense arms serve as the foundation for more extended, attenuated structures ($\rho \sim 10^8 m_p \text{ cm}^{-3}$) that are ionized and heated by EUV irradiation.

Different chemical species act as tracers for distinct regions within this outflowing atmosphere. Neutral Fe primarily probes the inner, rotation-dominated layers influenced by planetary spin and day-night circulation. The H α and He 10830 Å absorptions trace the interface between dense and attenuated gas in the spiral arms, where recombination of H $^+$ populates the 2s state of neutral hydrogen. Neutral Na, which survives in the dense spiral arms due to efficient recombination balancing FUV photoionization, exhibits significant velocity shifts (approximately 20 km s $^{-1}$ redshift during ingress and 35 km s $^{-1}$ blueshift during egress). These shifts, which are comparable to or exceed the planetary escape velocity, indicate that the large-scale spiral arm geometry and kinematics provide a more consistent explanation for the observed spectral line profiles than local super-rotation or other surface-bound phenomena.

The parametric study reveals the complex interactions between stellar radiation, atmospheric escape, and observable tracers. Enhanced FUV radiation drives more vigorous outflows but simultaneously photoionizes neutral sodium and metastable helium, leading to a non-linear response in absorption line strengths. Stronger EUV flux expands the spiral arm structures while effectively destroying neutral species, suppressing sodium features but significantly enhancing He 10830 Å absorption through increased recombination to the metastable state. Optical radiation primarily controls the outflow mass-loss rate by heating up the gas, while the inclusion of refractory grains as opacity sources also enhances atmospheric heating and escape. Strong stellar wind confinement compresses the dayside outflow, increasing local densities and recombination rates, which in turn strengthens both sodium and metastable helium absorption signatures. This demonstrates that metastable helium serves not only as an atmospheric escape tracer but also as a sensitive probe of wind-planet interactions.

The synergy between advanced numerical modeling and state-of-the-art observational instrumentation are promising to deepen our understanding of UHJs and planetary atmospheres in general. For instance, the extended He * trails observed by JWST for WASP-121b, which stretch well beyond the transit window (Allart

et al. 2025), can be self-consistently modeled within the Kratos framework by extending the simulation domain (e.g., to $r = 240 R_\oplus$ from the planet surface) and leveraging increased GPU computational resources. Simultaneous multi-wavelength observations of species that trace different atmospheric layers, such as He (from JWST) and Fe, H α , and Na (from ground-based facilities), will allow us to probe potential variability and chemical stratification in a coherent manner. This can be achieved by combining high-resolution spectrographs like KPF (Gibson et al. 2016), HISPEC (Konopacky et al. 2023) at the Keck Observatory, and PEPSI (Strassmeier et al. 2015) and iLocater (Crass et al. 2022) at the Large Binocular Telescope.

Time-resolved spectral monitoring during individual transits can reveal dynamical variability, such as the changing velocity patterns of neutral Fe lines reported by Ehrenreich et al. (2020); Lenhart et al. (2025); Basinger et al. (2025). Within the Kratos framework, such variability can be interpreted in terms of deeper atmospheric heating processes, potentially driven by opacity sources like carbon grains. Looking ahead, future extremely large telescopes (ELTs) will provide the spectral resolution, time resolution, and SNR that are necessary to detect short-term variability induced by hydrodynamic instabilities such as the Kelvin-Helmholtz instability (KHI) discussed in §3, offering insights into the real-time dynamics of exoplanetary upper atmospheres. Further inclusion of magnetic fields and non-ideal magnetohydrodynamic effects (whose magnetic diffusivity parameters are determined consistently by thermochemical calculations) could also open a new window for understanding the interplay between planetary outflows and stellar properties, and prospectively bridging the gap between global circulation models and microphysical escape processes.

ACKNOWLEDGMENTS

This work is supported by the National Natural Science Foundation of China (NSFC) under Grant 12573067. The computational resources supporting this work are provided by the Kavli Institute for Astronomy and Astrophysics, Peking University. We thank our colleagues: Fei Yan, Meng Sun, Wei Wang, Bin Ren, Jun Yang, Siyi Feng, for helpful discussions and suggestions on the contents of the paper.

REFERENCES

Allart, R., Coulombe, L.-P., Carteret, Y., et al. 2025, *Nature Communications*, 16, 10822, doi: [10.1038/s41467-025-66628-5](https://doi.org/10.1038/s41467-025-66628-5)

Arcangeli, J., Désert, J.-M., Line, M. R., et al. 2018a, *ApJ*, 855, L30, doi: [10.3847/2041-8213/aab272](https://doi.org/10.3847/2041-8213/aab272)

—. 2018b, *ApJ*, 855, L30, doi: [10.3847/2041-8213/aab272](https://doi.org/10.3847/2041-8213/aab272)

Arcangeli, J., Désert, J.-M., Parmentier, V., et al. 2019, *A&A*, 625, A136, doi: [10.1051/0004-6361/201834891](https://doi.org/10.1051/0004-6361/201834891)

Basinger, C., Johnson, M. C., Wang, J., et al. 2025, *MNRAS*, 543, 4136, doi: [10.1093/mnras/staf1648](https://doi.org/10.1093/mnras/staf1648)

Bell, T. J., & Cowan, N. B. 2018, *ApJ*, 857, L20, doi: [10.3847/2041-8213/aabcc8](https://doi.org/10.3847/2041-8213/aabcc8)

Borsa, F., Allart, R., Casasayas-Barris, N., et al. 2021, *A&A*, 645, A24, doi: [10.1051/0004-6361/202039344](https://doi.org/10.1051/0004-6361/202039344)

Changeat, Q., Edwards, B., Al-Refaie, A. F., et al. 2022, *ApJS*, 260, 3, doi: [10.3847/1538-4365/ac5cc2](https://doi.org/10.3847/1538-4365/ac5cc2)

Changeat, Q., Skinner, J. W., Cho, J. Y.-K., et al. 2024, *ApJS*, 270, 34, doi: [10.3847/1538-4365/ad1191](https://doi.org/10.3847/1538-4365/ad1191)

Christie, D., Arras, P., & Li, Z.-Y. 2013, *ApJ*, 772, 144, doi: [10.1088/0004-637X/772/2/144](https://doi.org/10.1088/0004-637X/772/2/144)

Crass, J., Aikens, D., Mason, J., et al. 2022, in Society of Photo-Optical Instrumentation Engineers (SPIE) Conference Series, Vol. 12184, Ground-based and Airborne Instrumentation for Astronomy IX, ed. C. J. Evans, J. J. Bryant, & K. Motohara, 121841P, doi: [10.1117/12.2630228](https://doi.org/10.1117/12.2630228)

Czesla, S., Nail, F., Lavaill, A., et al. 2024, *A&A*, 692, A230, doi: [10.1051/0004-6361/202451003](https://doi.org/10.1051/0004-6361/202451003)

Ehrenreich, D., Lovis, C., Allart, R., et al. 2020, *Nature*, 580, 597, doi: [10.1038/s41586-020-2107-1](https://doi.org/10.1038/s41586-020-2107-1)

Evans, T. M., Sing, D. K., Wakeford, H. R., et al. 2016, *ApJ*, 822, L4, doi: [10.3847/2041-8205/822/1/L4](https://doi.org/10.3847/2041-8205/822/1/L4)

Evans, T. M., Sing, D. K., Kataria, T., et al. 2017, *Nature*, 548, 58, doi: [10.1038/nature23266](https://doi.org/10.1038/nature23266)

Gaudi, B. S., Stassun, K. G., Collins, K. A., et al. 2017, *Nature*, 546, 514, doi: [10.1038/nature22392](https://doi.org/10.1038/nature22392)

Gibson, S. R., Howard, A. W., Marcy, G. W., et al. 2016, in Society of Photo-Optical Instrumentation Engineers (SPIE) Conference Series, Vol. 9908, Ground-based and Airborne Instrumentation for Astronomy VI, ed. C. J. Evans, L. Simard, & H. Takami, 990870, doi: [10.1117/12.2233334](https://doi.org/10.1117/12.2233334)

Hoeijmakers, H. J., Ehrenreich, D., Kitzmann, D., et al. 2019, *A&A*, 627, A165, doi: [10.1051/0004-6361/201935089](https://doi.org/10.1051/0004-6361/201935089)

Jacobs, B., Désert, J.-M., Pino, L., et al. 2022, *A&A*, 668, L1, doi: [10.1051/0004-6361/202244533](https://doi.org/10.1051/0004-6361/202244533)

Janev, R. K., Reiter, D., & Samm, U. 2003, Collision processes in low-temperature hydrogen plasmas, Berichte des Forschungszentrums Jülich

Kley, W., & Nelson, R. P. 2012, *ARA&A*, 50, 211, doi: [10.1146/annurev-astro-081811-125523](https://doi.org/10.1146/annurev-astro-081811-125523)

Komacek, T. D., & Tan, X. 2018, *Research Notes of the American Astronomical Society*, 2, 36, doi: [10.3847/2515-5172/aac5e7](https://doi.org/10.3847/2515-5172/aac5e7)

Konopacky, Q. M., Baker, A. D., Mawet, D., et al. 2023, arXiv e-prints, arXiv:2309.11050, doi: [10.48550/arXiv.2309.11050](https://doi.org/10.48550/arXiv.2309.11050)

Lee, E. K. H., Prinoth, B., Kitzmann, D., et al. 2022, *MNRAS*, 517, 240, doi: [10.1093/mnras/stac2246](https://doi.org/10.1093/mnras/stac2246)

Lendl, M., Csizmadia, S., Deline, A., et al. 2020, *A&A*, 643, A94, doi: [10.1051/0004-6361/202038677](https://doi.org/10.1051/0004-6361/202038677)

Lenhart, C., Johnson, M. C., Wang, J., et al. 2025, arXiv e-prints, arXiv:2503.07719, doi: [10.48550/arXiv.2503.07719](https://doi.org/10.48550/arXiv.2503.07719)

Lothringer, J. D., Barman, T., & Koskinen, T. 2018, *ApJ*, 866, 27, doi: [10.3847/1538-4357/aadd9e](https://doi.org/10.3847/1538-4357/aadd9e)

Lothringer, J. D., Fu, G., Sing, D. K., & Barman, T. S. 2020, *ApJ*, 898, L14, doi: [10.3847/2041-8213/aba265](https://doi.org/10.3847/2041-8213/aba265)

Mansfield, M., Line, M. R., Bean, J. L., et al. 2021, *Nature Astronomy*, 5, 1224, doi: [10.1038/s41550-021-01455-4](https://doi.org/10.1038/s41550-021-01455-4)

McElroy, D., Walsh, C., Markwick, A. J., et al. 2013, *A&A*, 550, A36

Müller, B., Tauris, T. M., Heger, A., et al. 2019, *MNRAS*, 484, 3307, doi: [10.1093/mnras/stz216](https://doi.org/10.1093/mnras/stz216)

Nakamura, K., Takiwaki, T., & Kotake, K. 2019, *PASJ*, 71, 98, doi: [10.1093/pasj/pzv080](https://doi.org/10.1093/pasj/pzv080)

Osterbrock, D. E., & Ferland, G. J. 2006, *Astrophysics of gaseous nebulae and active galactic nuclei* (University Science Books, Sausalito, CA)

Parmentier, V., Line, M. R., Bean, J. L., et al. 2018, *A&A*, 617, A110, doi: [10.1051/0004-6361/201833059](https://doi.org/10.1051/0004-6361/201833059)

Pelletier, S., Benneke, B., Chachan, Y., et al. 2025, *AJ*, 169, 10, doi: [10.3847/1538-3881/ad8b28](https://doi.org/10.3847/1538-3881/ad8b28)

Ramkumar, S., Gibson, N. P., Nugroho, S. K., Maguire, C., & Fortune, M. 2023, *MNRAS*, 525, 2985, doi: [10.1093/mnras/stad2476](https://doi.org/10.1093/mnras/stad2476)

Seidel, J. V., Ehrenreich, D., Wyttenbach, A., et al. 2019, *A&A*, 623, A166, doi: [10.1051/0004-6361/201834776](https://doi.org/10.1051/0004-6361/201834776)

Seidel, J. V., Borsa, F., Pino, L., et al. 2023, *A&A*, 673, A125, doi: [10.1051/0004-6361/202245800](https://doi.org/10.1051/0004-6361/202245800)

Seidel, J. V., Prinoth, B., Pino, L., et al. 2025, *Nature*, 639, 902, doi: [10.1038/s41586-025-08664-1](https://doi.org/10.1038/s41586-025-08664-1)

Sheppard, K. B., Mandell, A. M., Tamburo, P., et al. 2017, *ApJ*, 850, L32, doi: [10.3847/2041-8213/aa9ae9](https://doi.org/10.3847/2041-8213/aa9ae9)

Showman, A. P., Fortney, J. J., Lian, Y., et al. 2009, *ApJ*, 699, 564, doi: [10.1088/0004-637X/699/1/564](https://doi.org/10.1088/0004-637X/699/1/564)

Sing, D. K., Evans-Soma, T. M., Rustamkulov, Z., et al. 2024, *AJ*, 168, 231, doi: [10.3847/1538-3881/ad7fe7](https://doi.org/10.3847/1538-3881/ad7fe7)

Stevenson, K. B., Line, M. R., Bean, J. L., et al. 2017, AJ, 153, 68, doi: [10.3847/1538-3881/153/2/68](https://doi.org/10.3847/1538-3881/153/2/68)

Strassmeier, K. G., Ilyin, I., Järvinen, A., et al. 2015, Astronomische Nachrichten, 336, 324, doi: [10.1002/asna.201512172](https://doi.org/10.1002/asna.201512172)

Tan, X., & Komacek, T. D. 2019, ApJ, 886, 26, doi: [10.3847/1538-4357/ab4a76](https://doi.org/10.3847/1538-4357/ab4a76)

Wang, L. 2025a, ApJS, 277, 63, doi: [10.3847/1538-4365/adbdb6](https://doi.org/10.3847/1538-4365/adbdb6)

—. 2025b, arXiv e-prints, arXiv:2504.04941, doi: [10.48550/arXiv.2504.04941](https://doi.org/10.48550/arXiv.2504.04941)

Wang, L., & Dai, F. 2021a, ApJ, 914, 98, doi: [10.3847/1538-4357/abf1ee](https://doi.org/10.3847/1538-4357/abf1ee)

—. 2021b, ApJ, 914, 99, doi: [10.3847/1538-4357/abf1ed](https://doi.org/10.3847/1538-4357/abf1ed)

Xu, S., Wang, L., Ho, L. C., Cen, R., & Xu, S. 2026, ApJ, 997, 14, doi: [10.3847/1538-4357/ae2683](https://doi.org/10.3847/1538-4357/ae2683)

Yan, F., Pallé, E., Reiners, A., et al. 2022, A&A, 661, L6, doi: [10.1051/0004-6361/202243503](https://doi.org/10.1051/0004-6361/202243503)

Yang, F., Long, R. J., Liu, J.-f., et al. 2021, AJ, 161, 294, doi: [10.3847/1538-3881/abf92f](https://doi.org/10.3847/1538-3881/abf92f)